

VERY HIGH LORENTZ FACTOR FIREBALLS AND GAMMA-RAY BURST SPECTRA

KUNIHITO IOKA

KEK Theory Center and the Graduate University for Advanced Studies (Sokendai), Tsukuba 305-0801, Japan
Draft version July 8, 2018

ABSTRACT

Collisionless entrainment of the surrounding matter imports the relativistic baryon component in the Gamma-Ray Burst (GRB) fireball frame. We show that half the fireball energy can be transferred from radiation to the comoving hot motions of baryons under the photosphere. The yet baryon-poor fireball can reexpand to a very high Lorentz factor (VHLF) $\Gamma \sim 10^3$ – 10^6 by its own relativistic collisionless pressure beyond the photosphere (so-called collisionless bulk acceleration), leading to internal and external shocks. A simple synchrotron emission from the VHLF internal shocks produces (i) the extra power-law spectral component with variability observed in the Fermi GeV bursts, up to the TeV range for the future Cherenkov Telescope Array (CTA), (ii) the GeV onset delay with a weak luminosity dependence $t_{\text{delay}} \sim L^{-1/5}$, and (iii) the spectral break of GRB 090926 by the synchrotron cooling break or the maximum synchrotron cutoff limited by the dynamical time, not by the e^\pm creation cutoff. The relativistic baryon component could also heat the photospheric thermal photons into the main GRB Band spectrum via pp , $p\gamma$ (Bethe-Heitler and photomeson), and Coulomb thermalization processes. In this hot photosphere–internal–external shock model, we can predict the anticorrelation of \sim TeV neutrinos and GeV γ -rays, which may be detectable using IceCube. The spectral peak and luminosity (Yonetoku) relation is also reproduced if the progenitor stars are nearly identical. We also discuss the steep/shallow decay of early X-ray afterglows and short GRBs.

Subject headings: gamma rays: bursts — gamma rays: theory — radiation mechanism: non-thermal

1. INTRODUCTION

The cosmological Gamma-Ray Bursts (GRBs) are the most luminous objects in the Universe. Although the physical processes at the central engine are far from understood, the fireball model is generally accepted as the paradigm for producing the relativistic outflows and high-energy emission (Cavallo & Rees 1978; Paczyński 1986; Goodman 1986; Shemi & Piran 1990; Mészáros & Rees 1993a,b; Grimsrud & Wasserman 1998; Mészáros & Rees 2000a).

However, the actual emission mechanism of prompt GRBs is still debated, lacking a consistent picture. The main problem is the high efficiency ($\gtrsim 50\%$) of the GRB prompt emission, defined by the GRB energy divided by the total energy including the afterglow energy (Zhang et al. 2006; Ioka et al. 2006). With the use of the internal shock model (the leading model for the prompt emission), it is difficult to achieve a high efficiency without a large dispersion in the Lorentz factor of the outflows (Kobayashi et al. 1997; Kobayashi & Sari 2001; Beloborodov 2000). Even if it is achieved, a large dispersion in the Lorentz factor makes it difficult to realize the observed spectral relations (Zhang & Meszaros 2002), such as the Amati (Amati, Frontera & Guidorzi 2009; Amati 2010) and Yonetoku relations (Yonetoku et al. 2004; Kodama et al. 2008; Nava et al. 2010),

$$\varepsilon_{\text{peak}} \simeq 600 \left(\frac{L}{10^{53} \text{ erg s}^{-1}} \right)^{1/2} \text{ keV}, \quad (1)$$

where $\varepsilon_{\text{peak}}$ is the peak energy of the observed broken power-law spectrum (so-called the Band spectrum) and L is the apparent isotropic luminosity of the prompt emission observed within an angle $< 1/\Gamma$ of a jet axis. Such a correlation is also satisfied within individual pulses (Ohno et al. 2008; Ghirlanda et al. 2009). Another problem of the internal shock synchrotron model is that the low-energy spectral slope be-

comes steeper than that observed, owing to the intrinsic synchrotron spectrum and, even worse, owing to the fast electron cooling (Ghisellini et al. 2000a; Mészáros & Rees 2000a).

These difficulties of the internal shock models lead to the reexamination of the original fireball model (Paczynski 1986; Goodman 1986), in which photons are released as photospheric emission when the fireball becomes optically thin (Thompson 1994; Rees & Mészáros 2004; Thompson et al. 2007; Mészáros & Rees 2000a; Derishev et al. 1999; Mészáros et al. 2002; Pe’er & Waxman 2004; Thompson 2006; Pe’er et al. 2006; Ryde 2005; Giannios & Spruit 2007; Pe’er et al. 2007; Giannios 2008; Ioka et al. 2007; Ghisellini et al. 2007; Ryde & Pe’er 2009; Beloborodov 2009; Lazzati & Begelman 2010). The original problem is alleviated by introducing the dissipation under the photosphere (Rees & Mészáros 2004; Thompson et al. 2007), which can bring the thermal peak into the observed range in Eq. (1). The photosphere model can naturally achieve the high efficiency and the hard low-energy spectrum. The only flaw is that the spectrum tends to be thermal without nonthermal tails observed in GRBs, although a substantial fraction ($\sim 30\%$) of long GRBs may have thermal peaks (Ryde 2005; Ryde & Pe’er 2009). The nonthermal tails could arise from Comptonization of the thermal photons by electrons and positrons (e^\pm), heated at dissipation, such as magnetic reconnection (Giannios & Spruit 2007; Giannios 2008), neutron collisions (Derishev et al. 1999; Beloborodov 2009), or repeated shocks (Ioka et al. 2007; Lazzati & Begelman 2010). However, it seems questionable that a subdominant or a different component rather than the thermal component can supply the nonthermal energy that is accidentally comparable to the dominant thermal energy. Nevertheless, the photosphere model has an advantage that the peak energy $\varepsilon_{\text{peak}}$ is stabilized as it is fixed by the temperature of the photosphere, regardless of the dissipation mechanism. The spectral relations in Eq. (1) are more easily reproduced

(Rees & Mészáros 2004; Thompson et al. 2007) than the other attempts to solve the emission mechanism, such as the jitter radiation (Medvedev & Loeb 1999; Medvedev 2000), Klein-Nishina effect (Derishev et al. 2000; Bosnjak et al. 2009; Wang et al. 2010), synchrotron self-Compton (SSC) (Panaitescu & Mészáros 2000; Stern & Poutanen 2004), bulk Compton (Lazzati et al. 2000; Ghisellini et al. 2000b; Lazzati et al. 2004), decaying magnetic field (Rossi & Rees 2003; Pe’er & Zhang 2006), and quasi-thermal Comptonization (Ghisellini & Celotti 1999; Asano & Terasawa 2009).

Recently, the Fermi satellite, launched on 11 June 2008 with the GBM (8 keV – 40 MeV) and LAT (~ 20 MeV – 300 GeV) detectors, has been used to observe \sim GeV γ -rays from GRBs, providing interesting clues to the emission mechanism (Abdo et al. 2009a,b,c,d, 2010a,b,c). The GeV events are increasing more than sixfold from the era of EGRET that detected an 18 GeV photon 90 min after the burst in GRB 940217 (Hurley et al. 1994) and a rising late GeV spectral component in GRB 941017 (González et al. 2003). The main features of the Fermi bursts are summarized as follows:

- (1) In some Fermi/LAT bursts, the Lorentz factor of the outflows is constrained in the relatively high range $\Gamma \gtrsim 10^3$ so that the high-energy photons can avoid the annihilation by e^\pm pair creation (Abdo et al. 2009b,a, 2010c).
- (2) Fermi found an additional spectral component at $\gtrsim 10$ MeV with comparable energy to that of the main Band component, at least, in short GRB 090510 (Abdo et al. 2010c) and long GRB 090902B (Abdo et al. 2009a; Ryde et al. 2010). This extra component is fitted by a single power-law that slightly rises in $\nu F_\nu \propto \nu^{0.1-\nu^{0.4}}$ and often extends below $\lesssim 20$ keV over $\gtrsim 7$ energy digits. (However, note that no other experiments have confirmed the low-energy extension of the power-law component.)
- (3) The high-energy (> 100 MeV) emission lasts longer than the MeV emission in most LAT GRBs (Abdo et al. 2009d,b, 2010a, 2009a, 2010c). The well-observed extended emission shows a temporal power-law decay up to $\gtrsim 10^3$ s.
- (4) The high-energy emission sometimes shows a large amplitude variability on short timescales (Abdo et al. 2009a).
- (5) The high-energy emission is delayed behind the onset of the MeV emission in almost all LAT GRBs (Abdo et al. 2009d,b, 2010a, 2009a, 2010c). The delay time in the rest frame is $t_{\text{delay}} \sim 1$ s for long GRBs and ~ 0.1 s for short bursts, GRB 081024B and GRB 090510.
- (6) The prompt emission spectrum of GRB 090902B has a quasi-blackbody component, which is consistent with the photospheric emission (Abdo et al. 2009a; Ryde et al. 2010).

The Fermi discoveries excite the theoretical reconsiderations of the GeV emission, which may be classified as (i) the external shock models with synchrotron emission from adiabatic shocks (Kumar & Barniol Duran 2009a,b;

Barniol Duran & Kumar 2010; Corsi et al. 2009a,b; Gao et al. 2009; De Pasquale et al. 2010; Pandey et al. 2010) and radiative shocks (Ghirlanda et al. 2010; Ghisellini et al. 2010), SSC (Zou et al. 2009; Wang et al. 2010; Corsi et al. 2009a; Neamus 2010), and external Compton (Murase et al. 2010), and (ii) the internal shock models with synchrotron emission (Wang et al. 2009; Fan 2009), SSC (Li 2010a; Zou et al. 2009; Abdo et al. 2009a; Corsi et al. 2009a,b), hadronic emission (Asano et al. 2009a; Razzaque et al. 2009; Asano et al. 2009b), and external Compton of cocoon (Toma et al. 2009) or photospheric emission (Toma et al. 2010). The extended GeV emission most likely has the external shock origin. The emission mechanism could be other than synchrotron since the maximum synchrotron cutoff terminates the late ($\gtrsim 100$ s) emission of $\gtrsim 10$ GeV photons from external shock synchrotron (Li 2010b; Piran & Nakar 2010). On the other hand, the external shocks cannot produce the observed large amplitude variability on short timescales (Ioka et al. 2005; Sari & Piran 1997b), so that an additional origin, probably the internal shock emission, is also required. However, with the use of internal shock models, it is difficult to explain the hard extra component that extends to the low-energy excess. Obviously, synchrotron emission only cannot produce the extra component in addition to the Band component. The SSC emission usually peaks at higher energy than synchrotron without extending to the low-energy excess. Although hadronic models can make a low-energy excess via direct and cascade radiation (e.g., synchrotron emission by secondary pairs at low energies), the proton injection isotropic luminosity should be larger than 10^{55} erg/s, posing a challenge for these models (Asano et al. 2009b). The external Compton of cocoon (Toma et al. 2009) or photospheric emission (Toma et al. 2010) seems viable, but would need a fine tuning to smoothly connect the high- and low-energy excesses that have different emission origins in these models. Therefore, the prompt emission, not only the main Band component but also the extra component, remains a mystery.

In this paper, we revisit the dissipative photosphere model in light of the Fermi results, scrutinizing the dissipative processes that reproduce the spectral peak and luminosity (Yonetoku) relation in Eq. (1). We suggest that the dissipation is caused by the surrounding matter that decelerates the fireball (see §3.1). We show that the matter is loaded as the *relativistic* baryon component into the fireball, with a significant amount of energy received, comparable to that of the radiation component, using the energy and momentum conservation (see §3.2). This hitherto missing component can alter the fireball dynamics and spectra in a favorable way to solve the prompt emission. Firstly, if not fully thermalized as expected in the baryon-poor fireball, the relativistic baryon component can expand to a very high Lorentz factor (VHLF) $\Gamma \sim 10^3-10^6$ by its own relativistic collisionless pressure, via a so-called “collisionless bulk acceleration” mechanism (see §2 for a short summary). The subsequent VHLF internal shocks can explain the extra high-energy component with variability in the Fermi bursts by a single emission mechanism of synchrotron (see §4). Secondly, the relativistic baryon component could also operate as a heating source for e^\pm to Comptonize the photospheric thermal photons into the observed Band spectrum via pp , $p\gamma$ (Bethe-Heitler and photomeson), and Coulomb thermalization processes. Without fine tuning, the relativistic baryon component has the right amount of energy (comparable to the thermal energy) to make the nonthermal tails (see

§§3.2 and 5.2). In a sense, we consider a “hot photosphere” that is only partially thermalized with relativistic relic particles. Our picture falls into the photosphere–internal–external shock scenario (Toma et al. 2010), in which the main Band emission comes from the photosphere and the extra components come from the internal and external shocks.

This paper is organized as follows. In §2, we first summarize the basic idea for making the VHLF fireballs. In §3, we go into the fireball dynamics, expanding the idea of the collisionless bulk acceleration to a VHLF. In §3.1, we recall that the observed Yonetoku relation in Eq. (1) strongly suggests the fireball dissipation under the photosphere, probably caused by the baryon loading. In §3.2, we use a simple two-body collision to describe the dissipation, properly taking into account the relativistic hot motions of baryons before thermalization. We show that the relativistic baryon component naturally achieves comparable energy to the radiation. Then, after giving the photospheric and pionospheric radii in §3.3, we derive the final coasting Lorentz factor in §3.4. In §3.5, we examine the thermalization processes via $p\gamma$ (Bethe-Heitler and photomeson), Coulomb, and plasma interactions in addition to pp collisions. We devote §3.6 to consistency checks with previous works, and §3.7 to remarks on the connections between the collisionless bulk acceleration and the magnetic acceleration in making the VHLF fireballs.

Secondly, in §4, we apply the VHLF fireballs to the extra high-energy component with variability in the Fermi bursts. In §4.1, we firstly argue the GRB emission site in favor of the photosphere–internal–external shock scenario. In §4.2, we calculate the internal shock synchrotron spectrum in the VHLF models, which is found to be consistent with the observations, and also a nice target for the future Cherenkov Telescope Array (CTA), since the e^\pm creation cutoff goes beyond the TeV range in the VHLF models. In §4.3, we discuss the possible origins of the spectral break around ~ 1.4 GeV observed in the extra component of GRB 090926, which was suggested as the e^\pm creation cutoff for $\Gamma \sim 600$. In the VHLF models, the spectral break could be the synchrotron cooling break for $\Gamma \sim 10^4$, or the maximum synchrotron cutoff limited by the dynamical time, for $\Gamma \sim 10^5$. In §4.4, we suggest that the GeV onset delay and its weak dependence on the burst parameters can be naturally derived if the baryon loading at the dissipation is rich shortly after the jet break out of the progenitor star.

Finally, in §5, we discuss the future predictions and open issues. In §5.1, we predict the anticorrelation of \sim TeV neutrinos and GeV γ -rays, which might be detectable using IceCube. In §5.2, we suggest that the relativistic baryon component could transform the photospheric thermal photons into the observed Band spectrum. In §5.3, we go back to the origin of the Yonetoku relation in Eq. (1), which implies that the baryon loading rate, i.e., the environmental condition, is nearly identical to any bursts. In §5.4, we discuss possible configurations of the baryon loading. We also discuss the model implications for the steep/shallow decay of early X-ray afterglows in §5.6 and short GRBs in §5.7. We use the cgs units with $k_B = h = 1$ and $Q_x = Q/10^x$, and the standard cosmological parameters, $\Omega_m = 0.3$ and $\Omega_\Lambda = 0.7$, unless otherwise stated.

2. BASIC IDEA FOR VERY HIGH LORENTZ FACTOR (VHLF)

In this section, we briefly summarize the essence of the VHLF fireball formation, and clarify the connections between following sections.

Let us quickly recall the conventional fireball model

(Paczynski 1986; Goodman 1986; Shemi & Piran 1990; Mészáros & Rees 2000a). We initially consider a fireball that is compact and radiation-dominated. Since it is optically thick, the fireball expands by its own radiation pressure. The Lorentz factor grows as $\Gamma \propto r$, and is saturated at a constant Γ_c after almost all the radiation energy is converted into kinetic energy. The coasting Lorentz factor Γ_c is higher for lower baryon loads, whereas it has an upper limit for sufficiently low baryon loads because the fireball becomes optically thin in the accelerating phase before converting all the radiation energy into kinetic energy (i.e., before the saturation). The maximum value of the coasting Lorentz factor is about $\Gamma_c \leq \eta_* \sim 10^3$ for typical parameters [see Eq. (23) and §3.3].

Our idea is that even the baryon-poor fireball can accelerate to the saturating (very high) Lorentz factor, if the radiation energy is transferred to the other relativistic component that is not radiated away from the fireball. In our case, this is the relativistic baryon component (and the magnetic component resulting from it). We initially consider an almost baryon-free fireball (e.g., a leptonic fireball). A small amount of baryon is loaded into the fireball as the relativistic baryon component from the surrounding matter near the progenitor star or the preceding baryon-rich ejecta. The loaded baryon decelerates the fireball, receiving energy from the radiation in a collisionless way. We show that half the radiation energy can be transferred to the relativistic baryon component at the fireball dissipation using the energy and momentum conservation in Eqs. (11) and (12).

The fireball dissipation can occur under the photosphere (before the fireball becomes optically thin) so that the dissipated energy is trapped by the fireball. The dissipation is even demanded by the GRB observations if we identify the spectral peak energy $\varepsilon_{\text{peak}}$ with the fireball temperature (see §3.1 and Refs. Rees & Mészáros (2004) and Thompson et al. (2007)). The observed temperature $\Gamma T'$ drops at the dissipation because the fireball radius at the base of the flow r_b effectively increases, and this enables us to account for the observed spectral relations in Eq. (1) (see §§3.1 and 5.3). The thermalization of radiation and e^\pm is much faster than that of protons, keeping the comoving leptonic temperature at a non-relativistic value.

In previous studies, we usually (implicitly) assume that the baryon (proton) component of the fireball is also completely thermalized at the dissipation. This is the case (A) in Figs. 1 and 2, where we schematically show the fireball evolution with dissipation. The radiation-dominated fireball expands outward with $\Gamma \propto r$, and is dissipated, e.g., via shocks with baryon (protons) initially at rest. Here, if we look closely into the dissipation, the shock is usually collisionless at least in the early stage. The protons are trapped by the fireball via magnetic fields, which could be generated by the plasma instabilities or could be advected from the central engine. In any case, the velocity of protons is not changed so much in the frame of the shocked region. Then, the isotropized protons have a random Lorentz factor of

$$\gamma'_p \sim \Gamma_m (\sim 10^2 - 10^3), \quad (2)$$

in the shocked region because the protons drive into the shocked region with the Lorentz factor that is about the bulk Lorentz factor of the fireball after the merger Γ_m . In this process, the fireball energy is transferred to protons, leading to an almost equipartition of the (comoving) energy density be-

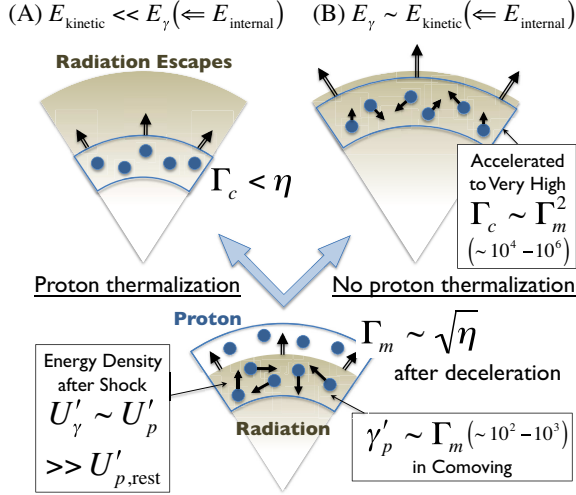


FIG. 1.— Schematic of a fireball evolution with dissipation. The radiation-dominated fireball is decelerated to a Lorentz factor $\Gamma_m \sim \sqrt{\eta}$ under the photosphere, via shock with baryon (protons) initially at rest. The comoving energy density of protons can be boosted to a value comparable to the radiation, $U'_p \sim U'_\gamma$, where almost all the proton energy is carried by the relativistic hot motions of protons with a random Lorentz factor of $\gamma'_p \sim \Gamma_m$. (A) If thermalization is effective, almost all the proton energy immediately dissipates into radiation, leading back to a standard radiation-dominated fireball. The maximum Lorentz factor is less than $\eta_* \sim 10^3$ as in the conventional case. (B) If thermalization is not effective, the relativistic collisionless motions of protons continue to push the fireball with $\Gamma \propto r$ up to a (saturating) VHLF, $\Gamma_c \sim \gamma'_p \Gamma_m \sim \eta \sim 10^3 - 10^6$, even beyond the photosphere. The kinetic energy remains comparable to the radiation energy since the energy density of relativistic protons behaves like radiation, $U'_p \sim U'_\gamma \propto r^{-4}$.

tween protons and radiation [see §3.2 and Eq. (18)],

$$U'_p \sim U'_\gamma, \quad (3)$$

according to the energy and momentum conservation in Eqs. (11) and (12). Thus, the kinetic luminosity temporarily equals the radiation luminosity, $L_k(A) \sim L_\gamma(A)$, in Fig. 2. The energy equipartition also renders the bulk Lorentz factor after the merger as

$$\Gamma_m \sim \sqrt{\eta}, \quad (4)$$

where η is the dimensionless entropy (the radiation to baryon ratio) of the fireball after the merger in Eq. (19). However, almost all the proton energy is carried by the relativistic hot motions of protons, not by the rest mass energy, i.e., $U'_{p,\text{rest}} \ll U'_p$. The subsequent thermalization of protons via pp , $p\gamma$ (Bethe-Heitler and photomeson), and Coulomb interactions (see §3.5) reduces the proton energy and pressure considerably into radiation [For example, the protons are effectively thermalized via pp collisions under the pionsphere $r < r_{pp}$, where the optical depth to pp collisions is larger than unity $\tau_{pp} > 1$ (see §3.3)]. Then, the fireball evolution is essentially similar to that without shocks since the dissipated energy is trapped in the system under the photosphere. Therefore, the coasting Lorentz factor has a conventional upper limit of

$$\Gamma_c \leq \eta_* \sim 10^3, \quad (5)$$

as the radiation escapes from the photosphere before transferring its energy to the baryon kinetic energy [see Eq. (23) and §3.3].

The evolution is totally different if the thermalization is not completed. This is the case (B) in Figs. 1 and 2. The evo-

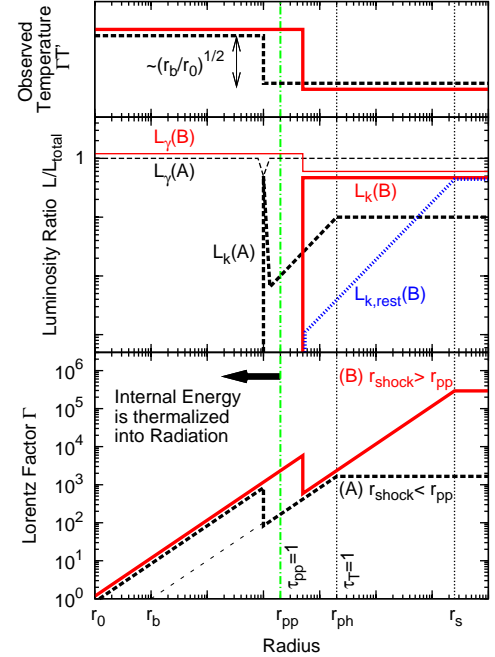


FIG. 2.— Schematic evolution of physical quantities as a function of the fireball radius r . The radiation-dominated fireball is decelerated via shock with baryon (protons) initially at rest, boosting the proton energy to a value comparable to the radiation. (A) (dashed lines) If the thermalization is effective, e.g., under the pionsphere $r < r_{pp}$ with the pp collisional optical depth $\tau_{pp} > 1$, almost all the proton kinetic luminosity $L_k(A)$ immediately dissipates into the radiation luminosity $L_\gamma(A)$. The Lorentz factor grows under the radiation pressure, so that it coasts at the photosphere $r = r_{ph}$ with $\Gamma_c \lesssim 10^3$. (B) (solid lines) If the protons are not thermalized, the kinetic luminosity remains comparable to the radiation luminosity, $L_k(B) \sim L_\gamma(B)$, since almost all the proton energy is carried by the relativistic random motions of protons, not by the rest mass energy, $L_{k,\text{rest}}(B) \ll L_k(B)$. The Lorentz factor grows under the proton collisionless pressure up to a VHLF, $\Gamma_c \sim \Gamma_m^2 \sim 10^3 - 10^6$, even beyond the photosphere $r > r_{ph}$. In both cases (A) and (B), the observed temperature $\Gamma T'$ drops by $\sim (r_b/r_0)^{1/2}$ times because the fireball radius at the base of the flow r_b effectively increases.

lution is almost the same as the previous case (A) before the proton thermalization. However, if the relativistic hot motions of protons are not thermalized (e.g., pp collisions are not effective with $\tau_{pp} < 1$), the relativistic collisionless motions of protons reexpand the fireball with $\Gamma \propto r$, acting like radiation pressure. Since the random motions are converted into the bulk motion, the final bulk Lorentz factor is the bulk Lorentz factor after the merger Γ_m multiplied by the random Lorentz factor $\gamma'_p \sim \Gamma_m$ as

$$\Gamma_c \sim \gamma'_p \Gamma_m \sim \Gamma_m^2 \sim \eta \quad (\sim 10^4 - 10^6), \quad (6)$$

which is a (saturating) VHLF, much larger than the conventional upper limit $\eta_* \sim 10^3$ in Eqs. (5) and (23). It is remarkable that such a “collisionless bulk acceleration” continues beyond the photosphere, $r > r_{ph}$, i.e., even after radiation loses contact with matter, in contrast with the thermalization case (A). The kinetic luminosity also remains comparable to the radiation luminosity,

$$L_k(B) \sim L_\gamma(B), \quad (7)$$

since the energy density of relativistic protons behaves like radiation, $U'_p \sim U'_\gamma \propto r^{-4}$.

The energy source of the collisionless bulk acceleration is the initial radiation energy. The radiation energy is transferred to the relativistic baryon component in the nonradiative form

of the isotropic random hot motions, which is later converted into the bulk kinetic energy. Even if the relativistic baryon energy dissipates into the magnetic field, a similar acceleration continues via the magnetic pressure (see §§3.5 and 3.7). However, the acceleration mechanism does not work if the baryon loading occurs after the coasting since adding mass just reduces the bulk Lorentz factor.¹

According to the above considerations, it is physically reasonable to define a VHLF as a Lorentz factor larger than the conventional maximum value $\eta_* \sim 10^3$ in Eqs. (5) and (23). A VHLF could open a new paradigm for interpreting the GRB properties, removing a theoretical bias to the lower Lorentz factors. In §4, we apply the VHLF fireballs to the internal shock synchrotron model for reproducing the keV–GeV power-law spectrum with high time variability detected by Fermi (§4.2), the spectral break in GRB 090926 by the synchrotron cooling break or the maximum synchrotron cutoff limited by the dynamical time (§4.3), and the GeV onset delay (§4.4). In §4, we predict an anticorrelation between GeV γ -rays and TeV neutrinos, and also suggest that the relativistic baryon component could heat the photospheric thermal photons into the observed Band spectrum.

Note that each element of our idea to create VHLF fireballs is not completely new. The acceleration, which converts the internal energy back into the kinetic energy, was previously discussed in the context of the internal shock efficiency (Kobayashi & Sari 2001; Kumar 1999), although their fireballs cannot reach a VHLF since shocks occur in the coasting phase, not in the accelerating phase. The fireball dissipation under the photosphere was also discussed in the photosphere model (Rees & Mészáros 2004; Thompson et al. 2007; Ghisellini et al. 2007; Ioka et al. 2007). The pionosphere was also discussed for the neutrino emission and the neutron decoupling (Mészáros & Rees 2000b; Paczyński & Xu 1994; Derishev et al. 1999; Fuller et al. 2000; Beloborodov 2009). However, the combination of these elements leads to a new concept of the VHLF fireball arising from the hot photosphere, which has not been discussed so far, to the best of our knowledge.

It is useful to refer to an interesting analogy with cosmology. The relativistic protons that are not thermalized after the fireball dissipation are similar to the relic particles in the Universe, in particular, hot relics such as neutrinos and light dark matter, which are relativistic at the freeze out. In this sense, a “hot relic fireball” attains a VHLF. The dissipation of the GRB fireball is also similar to the reheating of the Universe, both of which leads to the entropy production after the birth of the fireball. We use “dissipation” for both the entropy production at the collisionless shock and at the thermalization of relativistic protons, and “thermalization” for the dissipation of the relativistic proton energy into radiation.

3. FIREBALL DYNAMICS: COLLISIONLESS BULK ACCELERATION TO VERY HIGH LORENTZ FACTOR (VHLF)

In this section, we investigate the fireball dynamics to a VHLF via collisionless bulk acceleration in detail, extending the idea in the previous section. In §3.1, we first recall that the fireball dissipation is strongly suggested by the observed spectral relation. We suggest that the dissipation is caused

by the mass loading, not by the magnetic reconnection or neutron decay, for the radiation-dominated fireball. In §3.2, we use a simple two-body collision to describe the dissipation, properly taking into account the relativistic hot motions of protons before thermalization to discuss the collisionless bulk acceleration. Then, after giving the photospheric and pionospheric radii in §3.3, we derive the final coasting Lorentz factor in §3.4. In §3.5, we examine thermalization processes [$p\gamma$ (Bethe-Heitler and photomeson), Coulomb, and plasma interactions] other than pp collisions, which are relevant in some circumstances. We devote §3.6 to consistency checks with previous works, and §3.7 to remarks on the connections between the collisionless bulk acceleration and the magnetic acceleration in making the VHLF fireballs.

3.1. Fireball dissipation suggested by $\varepsilon_{\text{peak}}-L$ Yonetoku relation

The photosphere model has many advantages for interpreting the GRB prompt emission (see §1). In this model, we identify the spectral peak energy $\varepsilon_{\text{peak}}$ with the fireball photospheric temperature T . The fireball is likely radiation-dominated since the radiative efficiency is high in most GRBs. Under these assumptions, the fireball dissipation is strongly suggested by the observed spectral relation, i.e., the $\varepsilon_{\text{peak}}-L$ Yonetoku relation in Eq. (1), as pointed out by Thompson et al. (2007) (Thompson et al. 2007; Pe’er et al. 2007) (see below).

In the usual picture that the engine is an accreting black hole or possibly a rapidly rotating magnetar, the engine size r_0 is essentially constant about a couple of Schwarzschild radii $r_0 \sim 10^7$ cm for a black hole of mass $M_{\text{BH}} \sim 10M_{\odot}$. However, this picture ($r_0 \sim \text{const}$) leads to a different relation for the isotropic luminosity,

$$L = 4\pi r_0^2 c a T_0^4 \propto T^4, \quad (8)$$

from the observed Yonetoku relation $L \propto T^2$, where the observed temperature preserves the initial temperature $T \sim T_0$ for radiation-dominated fireballs. Therefore, the fireball radius is most likely reset by the fireball dissipation. Note that the relation tracks $L \propto T$ after the fireball becomes matter-dominant. Although we might be able to transform $L \propto T^4$ to $L \propto T^2$ by using the matter-dominant track, this is not likely since the low-luminosity region becomes radiatively too inefficient.

The dissipation takes place at a radius that is much larger than the engine radius r_0 . We may estimate the radius of the dissipated fireball at the base of the flow by using the black body relation $L = 4\pi(r_{\text{ph}}/\Gamma_{\text{ph}})^2 c a T^4$ as

$$r_b \equiv \frac{r_{\text{ph}}}{\Gamma_{\text{ph}}} \sim 1 \times 10^8 \text{ cm } L_{53}^{1/2} T_{600\text{keV}}^{-2} > r_0 \sim 10^7 \text{ cm}, \quad (9)$$

where r_{ph} is the photospheric radius, Γ_{ph} is the Lorentz factor of the radiating flow, and we have $r_b \propto L^{-1/2}$ if we also combine the Yonetoku relation in Eq. (1).

In general, the actual dissipation radius $r_m \sim \Gamma_m r_b$ is larger than the base radius r_b , because, in order to be observed, a fireball has to have a relativistic bulk Lorentz factor Γ_m after the dissipation (see §3.2; Note that, by definition, the Lorentz factor is unity as pulled back to the base of the flow with $\Gamma \propto r$). The dissipation radius r_m may be comparable to the size of the progenitor star $r_m \sim \Gamma_m r_b \sim 10^{10}-10^{11}$ cm if $\Gamma_m \sim 10^2-10^3$. Actually, such dissipation is suggested by numerical simulations as the jet interacts with the progenitor star (Lazzati et al.

¹ In this paper, we consider the complete merger case. If we consider the reverse and forward shock structure, the further acceleration is seemingly repeatable even after the coasting since the energy can be transferred from the rear to the front shell. However, this is not likely as the front shell reaccelerates before completely receiving the rear shell energy [see §5.4 and Eq. (84)].

2009; Zhang et al. 2004; Mizuta et al. 2004, 2010) (see also §§5.3 and 5.4).

In addition, the dissipation has to be associated with the deceleration of the fireball. For an impulsive dissipation like shocks, the bulk Lorentz factor has to be decelerated by $\sim r_b/r_0 \sim 10 L_{53}^{-1/2}$ times at the dissipation, and for a continuous dissipation, the total change of the bulk Lorentz factor would be of the same order, because $\Gamma \propto r$ for radiation-dominated fireballs (see Fig. 2). For the fireball to be decelerated, the dissipation seems to be caused by the mass loading, probably the baryon loading, not by the magnetic reconnection or the neutron decay (see also §§5.3 and 5.4).

3.2. Initial condition of dissipated fireballs

As we have discussed in the previous section, the $\varepsilon_{\text{peak}}\text{-}L$ Yonetoku relation suggests the fireball dissipation under the photosphere due to the baryon loading. The main features of the dissipation can be described by a simple two-body collision. In contrast to the previous calculations, we approximately take into account the relativistic hot motions of protons to discuss the collisionless bulk acceleration.

We consider a rapid shell that is radiation-dominated with internal energy E'_r ($\propto r^{-1}$) and Lorentz factor Γ_r ($\propto r$) $\gg 1$, merging with a slow mass M_s with a Lorentz factor Γ_s . Here, $\Gamma_s = 1$ for the matter located near the progenitor star, and $\Gamma_s > 1$ for internal shocks. The total energy in the lab frame is also rewritten as

$$E'_r \Gamma_r = L_j t_v, \quad (10)$$

using the duration t_v and the geometry-corrected jet luminosity $L_j = L(\theta_j/2)^2$. We assume no baryon in the rapid shell for simplicity. Although radiation may be already decoupled from the baryon-poor rapid shell before the merger, the radiation is trapped again by the merged shell if the radius is under the photosphere.

The energy and momentum conservation gives

$$E'_r \Gamma_r + M_s c^2 \Gamma_s = (\Gamma_{ms} M_s c^2 + E'_m) \Gamma_m, \quad (11)$$

$$E'_r \sqrt{\Gamma_r^2 - 1} + M_s c^2 \sqrt{\Gamma_s^2 - 1} = (\Gamma_{ms} M_s c^2 + E'_m) \sqrt{\Gamma_m^2 - 1} \quad (12)$$

where E'_m and Γ_m are the internal energy and the bulk Lorentz factor after the merger, respectively, and

$$\Gamma_{ms} = \Gamma_m \Gamma_s - \sqrt{\Gamma_m^2 - 1} \sqrt{\Gamma_s^2 - 1} \quad (13)$$

is the relative Lorentz factor between Γ_m and Γ_s . The point different from the previous studies is that we take into account the prethermalized relativistic motions of protons with Γ_{ms} in Eqs. (11) and (12). Of course, this treatment is approximate but valid for order-of-magnitude estimates. If we consider in the rest frame of the shocked region, the protons run into the shocked region with $\sim \Gamma_{ms}$ and are isotropized by magnetic fields. Here, weak magnetization is sufficient to trap protons, and the magnetic fields could be generated by the plasma instabilities or could be advected from the central engine. Since the shock is collisionless for protons before thermalization, the proton velocities are not altered so much in the frame of the shocked region. Therefore, the random Lorentz factor of protons would also be about Γ_{ms} in the shocked region. Before the complete deceleration, the relative Lorentz factor between the preshocked protons and the shocked region is larger than Γ_{ms} . Thus, a fraction of protons would have the random

Lorentz factor larger than Γ_{ms} . However, at least half of the protons are shocked after the shocked region is well decelerated, thereby having the random Lorentz factor of $\sim \Gamma_{ms}$. We do not consider the particle acceleration at the shock for simplicity.

We can solve two equations, Eqs. (11) and (12), for two unknowns, Γ_m and E'_m , as

$$\Gamma_m = \frac{E'_r \Gamma_r + M_s c^2 \Gamma_s}{\sqrt{E_r'^2 + M_s^2 c^4 + 2E'_r M_s c^2 \Gamma_{rs}}}, \quad (14)$$

$$E'_m = \sqrt{E_r'^2 + M_s^2 c^4 + 2E'_r M_s c^2 \Gamma_{rs}} - \Gamma_{ms} M_s c^2, \quad (15)$$

where $\Gamma_{rs} = \Gamma_r \Gamma_s - \sqrt{\Gamma_r^2 - 1} \sqrt{\Gamma_s^2 - 1}$ is the relative Lorentz factor between rapid and slow shells, and $\Gamma_{rs} \sim \Gamma_r/2\Gamma_s$ for $\Gamma_r \gg 1$.

We are now considering the following case:

- (i) the energy is dominated by the rapid shell, $E'_r \Gamma_r \gg M_s c^2 \Gamma_s$, so that $E'_r \Gamma_{rs} \gg M_s c^2$ and also the merged shell is still relativistic $\Gamma_m \gg 1$, i.e., $\Gamma_{ms} \sim \Gamma_m/2\Gamma_s$,
- (ii) the rapid shell decelerates effectively $\Gamma_m < \Gamma_r/2$, converting the kinetic energy into the internal energy, so that $2M_s c^2 \Gamma_{rs} \gg E'_r$.

That is, the slow mass is in the range,

$$10^{-11} M_\odot L_{53} \theta_j^2 t_{v,-3} \Gamma_{r,3}^{-2} \Gamma_s^2 \ll M_s \Gamma_s \ll 10^{-5} M_\odot L_{53} \theta_j^2 t_v, \quad (16)$$

with Eq. (10), and thereby, only a small fraction of the progenitor mass is sufficient to decelerate the fireball efficiently. Then, we can simplify Eqs. (14) and (15) as

$$\Gamma_m \sim \left(\frac{E'_r \Gamma_r \Gamma_s}{M_s c^2} \right)^{1/2} = \sqrt{\Gamma_s \eta}, \quad (17)$$

$$E'_m \sim \Gamma_{ms} M_s c^2, \quad (18)$$

where we use Eq. (10) in the last equality in Eq. (17), and introduce a dimensionless entropy (the radiation-to-baryon ratio) of the fireball after the merger as

$$\eta \equiv \frac{E'_r \Gamma_r}{M_s c^2} = \frac{L_j t_v}{M_s c^2} \equiv \frac{L}{\dot{M} c^2}. \quad (19)$$

Equations (17) and (18) have important implications for the initial condition of the dissipated fireballs:

- First, we can interpret Eq. (18) that the proton energy is boosted to a value comparable to the radiation E'_m and almost all the proton energy $\Gamma_{ms} M_s c^2$ is carried by their relativistic hot motions with the Lorentz factor

$$\gamma'_p \sim \Gamma_{ms} \sim \frac{\Gamma_m}{2\Gamma_s}. \quad (20)$$

- Second, if the relativistic hot motions are converted into the bulk motion, the final bulk Lorentz factor achieves the saturation level,

$$\Gamma_c \sim \Gamma_m \gamma'_p \sim \frac{\Gamma_m^2}{2\Gamma_s} \sim \frac{\eta}{2}, \quad (21)$$

with Eqs. (17) and (20), so that the kinetic luminosity becomes comparable to the total luminosity, $\Gamma_c \dot{M} c^2 \sim L/2$.

- Finally, the fireballs should be relativistic even after the dissipation in order to produce the observed GRBs; otherwise, the final Lorentz factor cannot be sufficiently high, $\Gamma_c > 10^2\text{--}10^3$, to avoid the compactness problem.

Note that the bulk Lorentz factor after the merger Γ_m is the same as Eq. (17) even if we omit the new factor Γ_{ms} in Eqs. (11) and (12) as in the conventional case.

3.3. Photosphere and pionosphere of fireballs

In this section, we summarize several important radii of the fireballs, in particular, for the photosphere and pionosphere (Rees & Mészáros 2004; Mészáros & Rees 2000a; Mészáros et al. 2002) to derive the final coasting Lorentz factor in the next section. We assume that the fireballs are created intermittently with a variability timescale $t_v \simeq r_b/c$, which is determined by the size at the base of the flow, for simplicity, although we may apply the following arguments as long as the timescale is longer than the causal timescale, $t_v > r/c\Gamma^2$.

Baryonic photosphere r_{ph} is determined by $\tau_T = 1$, where the Thompson optical depth to electrons associated with protons, $\tau_T = n'_p \sigma_T r / \Gamma$, is unity.² The Lorentz factor is $\Gamma = [r/r_b, \eta]$, the comoving width of the shell is $\Delta' = [r, r_b\eta]$, and the comoving volume of the shell is $V' = 4\pi r^2 \Delta' = [4\pi r^3, 4\pi \eta r_b r^2]$ when the radius r is $[< r_b\eta, > r_b\eta]$. Then, with the baryon density $n'_p = L t_v / \eta m_p c^2 V'$, we can derive the photospheric radius as

$$\frac{r_{\text{ph}}}{r_b} = \begin{cases} \eta_*^{4/3} \eta^{-1/3} & \text{for } \eta > \eta_* \\ \eta_*^4 \eta^{-3} & \text{for } \eta < \eta_*, \end{cases} \quad (22)$$

where

$$\eta_* = \left(\frac{L \sigma_T}{4\pi m_p c^3 r_b} \right)^{1/4} \simeq 1 \times 10^3 L_{53}^{1/4} r_{b,8}^{-1/4} \quad (23)$$

is a critical dimensionless entropy. We can apply the above relations to the wind regime, $r \gtrsim ct, \eta^2 \simeq r_b \eta^2$, where the successive shells expand their thickness and overlap through internal shocks, because $n'_p = L / 4\pi r^2 m_p c^3 \eta \Gamma$ and the Lorentz factor is saturated at $r = r_b \eta$ with $\Gamma = \eta$.

Pionosphere is defined by $\tau_{pp} = 1$, where the optical depth to pp collisions (i.e., pionic optical depth) is unity. Repeating the previous calculations, we have

$$\frac{r_{pp}}{r_b} = \begin{cases} \eta_{pp}^{4/3} \eta^{-1/3} & \text{for } \eta > \eta_{pp} \\ \eta_{pp}^4 \eta^{-3} & \text{for } \eta < \eta_{pp}, \end{cases} \quad (24)$$

where

$$\eta_{pp} = \left(\frac{L \sigma_{pp}}{4\pi m_p c^3 r_b} \right)^{1/4} = \left(\frac{\sigma_{pp}}{\sigma_T} \right)^{1/4} \eta_* \simeq 500 L_{53}^{1/4} r_{b,8}^{-1/4} \quad (25)$$

An e^\pm photosphere can be formed beyond the baryonic photosphere (Pilla & Loeb 1998; Guetta et al. 2001; Kobayashi et al. 2002; Mészáros et al. 2002; Li et al. 2003; Rees & Mészáros 2004; Ioka et al. 2007). Although there are some uncertainties in the amount of e^\pm , the actual e^\pm abundance will be between the following three cases:

(1) The e^\pm - p equal mass case, in which the rest mass energy density of e^\pm is equal to that of baryon. We can obtain the e^\pm

photospheric radius r_\pm by replacing m_p and m_e in the baryonic photosphere case as

$$\frac{r_\pm}{r_b} = \begin{cases} \eta_\pm^{4/3} \eta^{-1/3} & \text{for } \eta > \eta_\pm \\ \eta_\pm^4 \eta^{-3} & \text{for } \eta < \eta_\pm, \end{cases} \quad (26)$$

where

$$\eta_\pm = \left(\frac{L \sigma_T}{4\pi m_e c^3 r_b} \right)^{1/4} = \left(\frac{m_p}{m_e} \right)^{1/4} \eta_* \simeq 7 \times 10^3 L_{53}^{1/4} r_{b,8}^{-1/4} \quad (27)$$

(2) The feasible case, in which the e^\pm density is determined by the balance between e^\pm annihilation and creation, where e^\pm is created by pp collisions. This is guaranteed in the presence of relativistic hot protons, which remains not thermalized after the fireball dissipation.

The inelastic cross section for pp collisions is about $\sigma_{pp} \sim 3 \times 10^{-26} \text{ cm}^2$ above the pion production threshold $\sim 140 \text{ MeV}$. The inelasticity K_{pp} is ~ 0.5 , so only a few collisions are required to extract most of the energy of the primary particles. The energy is initially given to produce π^\pm and π^0 , where the π multiplicity is typically $\mathcal{M}_\pi \sim 1\text{--}3$ near the threshold $\sqrt{s} \sim 1 \text{ GeV}$ and weakly depends on the center-of-mass energy as $\mathcal{M}_\pi \propto \ln \sqrt{s}$ (Grosse-Oetringhaus & Reygiers 2009). The pions immediately decay as $\pi^+ \rightarrow \mu^+ + \nu_\mu \rightarrow e^+ + \nu_e + \bar{\nu}_\mu + \nu_\mu$, $\pi^- \rightarrow \mu^- + \bar{\nu}_\mu \rightarrow e^- + \bar{\nu}_e + \nu_\mu + \bar{\nu}_\mu$, and $\pi^0 \rightarrow \gamma + \gamma$, and the decay gamma-rays create e^\pm via $\gamma\gamma$ interactions. Thus, the minimum e^\pm multiplicity without considering the following cascade is

$$\mathcal{M}_\pm^{\text{min}} \sim 2\mathcal{M}_\pi. \quad (28)$$

Alternatively, since the injected e^\pm has a large Lorentz factor $\gamma'_\pm \sim K_{pp} \gamma'_p m_p / 2\mathcal{M}_\pi m_e$, the electromagnetic cascade will follow and could achieve the maximum e^\pm multiplicity,

$$\mathcal{M}_\pm^{\text{max}} \sim K_{pp} \gamma'_p m_p / m_e, \quad (29)$$

where γ'_p is the comoving Lorentz factor of protons. The minimum e^\pm multiplicity would be appropriate when the synchrotron cooling dominates, since the synchrotron photons are typically soft $\lesssim 1 \text{ MeV}$, while the maximum e^\pm multiplicity would be valid when the inverse Compton cooling dominates, since the relativistic e^\pm can scatter photons to high-energy $\gg 1 \text{ MeV}$. Hereafter, we parametrize the e^\pm multiplicity as

$$\mathcal{M}_\pm = f_\pm \gamma'_p m_p / m_e. \quad (30)$$

Then, equating the annihilation rate

$$\dot{n}'_\pm = \frac{3}{8} n'_+ n'_- \sigma_T c \quad (31)$$

with the creation rate

$$\dot{n}'_\pm = \mathcal{M}_\pm n'^2_p \sigma_{pp} c, \quad (32)$$

we obtain the feasible e^\pm density $n_\pm = n_+ \sim n_-$ as

$$\frac{n'_\pm}{n'_p} = \left(\frac{8 \sigma_{pp} m_p}{3 \sigma_T m_e} f_\pm \gamma'_p \right)^{1/2}, \quad (33)$$

which can be much larger than unity.

(3) The maximum case, in which the comoving radiation energy is almost converted to the e^\pm rest mass energy. This extreme case might be realized if the radiation spectrum has

² In Ref. Mészáros et al. (2002), $\tau_T = n' \sigma_T \Delta'$ was used in the discrete shell regime. However, we think that $\tau_T = n' \sigma_T r / \Gamma$ is correct since photons can travel only a distance $\sim r / \Gamma$ within the comoving time at radius r .

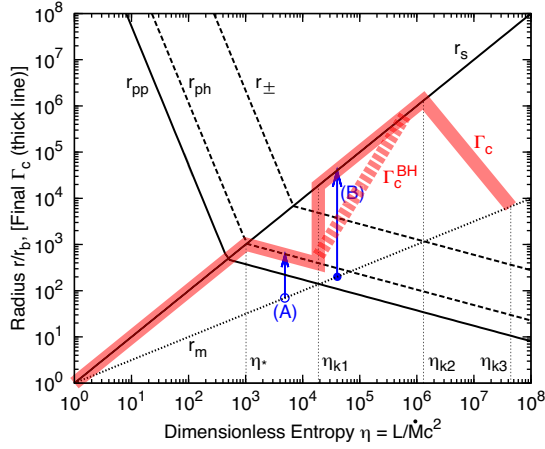


FIG. 3.— η - r diagram to read normalized radii r/r_b and the final coasting Lorentz factor Γ_c in Eq. (39) (red thick line) and in Eq. (47) (with efficient Bethe-Heitler processes; red thick dotted line) as a function of the dimensionless entropy $\eta = L/Mc^2$ (the radiation to baryon ratio). A fireball can achieve a VHLF, $\Gamma_c > \eta_*$, if the dissipation radius r_m in Eq. (35) exceeds the photosphere r_{pp} in Eq. (22) (pionic optical depth $\tau_{pp} = 1$). The maximum coasting Lorentz factor reaches $\Gamma_{c,\max} \sim 10^6$ in Eqs. (41) and (42). We also show the baryonic photosphere r_{ph} in Eq. (24) (Thompson optical depth $\tau_T = 1$), the e^\pm photosphere r_\pm in Eq. (26) for the e^\pm - p equal mass case, and the saturation radius $r_s/r_b = \eta$. Critical entropies η_* , η_{k1} , η_{k2} , and η_{k3} are given by Eqs. (23), (36), (37), and (38), respectively.

a significant fraction of energy above the pair production threshold and the e^\pm pairs develop an electromagnetic cascade. With the e^\pm density $n'_{\pm,\max} = Lt_v/\Gamma m_e c^2 V'$, the optical depth condition $\tau_T = n'_{\pm,\max} \sigma_T r/\Gamma = 1$ gives

$$\frac{r_{\pm,\max}}{r_b} = \begin{cases} \eta_\pm & \text{for } \eta > \eta_\pm \\ \eta_\pm^4 \eta^{-3} & \text{for } \eta < \eta_\pm. \end{cases} \quad (34)$$

The e^\pm rest mass energy surpasses the baryonic one, because the proton energy, comparable to the radiation energy in Eq. (18), is carried by relativistic motions, not by the rest mass energy. The acceleration terminates at this radius $r_{\pm,\max}$ since the e^\pm rest mass energy almost equals the total energy.

3.4. Final coasting Lorentz factor of dissipated fireballs

Figure 3 shows the η - r diagram, (Rees & Mészáros 1994; Mészáros & Rees 2000a,b) which is useful to read out the final coasting Lorentz factor. In the conventional picture, we usually start the fireball evolution from the base of the flow, $r/r_b = 1$, for a given entropy η . The fireball expands with $\Gamma \propto r$ as far as below the saturation radius r_s and the photospheric radius r_{ph} . Then, the maximum coasting Lorentz factor is $\sim \eta_*$ in Eq. (23).

However, the starting radius is different from the base, $r/r_b = 1$, for the dissipated fireball case because the observed fireballs have to be relativistic after dissipation, as discussed in §3.2. Then, using $\Gamma \propto r$, we can plot the starting radius r_m in the diagram (dotted line in Fig. 3) as

$$\frac{r_m}{r_b} \sim \Gamma_m \sim \sqrt{\Gamma_s \eta}, \quad (35)$$

where Γ_m is the bulk Lorentz factor after dissipation in Eq. (17), derived from the energy and momentum conservation in Eqs. (11) and (12), and Fig. 3 shows the case $\Gamma_s = 1$. Here, we take the independent model parameters as the dimensionless entropy η in Eq. (19), the Lorentz factor of the slow mass Γ_s , the total isotropic luminosity L , and the engine

size r_0 ($< r_b$) in §3.1. We can derive the other parameters, such as the observed temperature T in Eq. (1), the radius at the base of the flow r_b in Eq. (9), the dissipation radius r_m in Eq. (35), and the Lorentz factor of the rapid shell before merger $\Gamma_r = r_m/r_0$.

As long as the dissipation radius is below the photosphere, $r_m < r_{pp}$, i.e., in the low to moderate entropy range $\eta < \eta_{k1}$ (see Fig. 3) where

$$\eta_{k1} = \Gamma_s^{-3/5} \eta_{pp}^{8/5} \simeq 2 \times 10^4 \Gamma_s^{-3/5} L_{53}^{2/5} r_{b,8}^{-2/5}, \quad (36)$$

with Eqs. (24) and (35), the fireball evolution is essentially similar to the conventional case. This is the case (A) in Fig. 3. The relativistic hot motions of protons, acquired at the merger with a radiation-dominated fireball, are quickly thermalized into radiation via pp collisions under the photosphere. The dissipated fireball goes back to the standard radiation-dominated fireball, and hence, the maximum coasting Lorentz factor is again $\sim \eta_*$ in Eq. (23), as the radiation escapes from the photosphere $r = r_{ph}$. Such a fireball is sometimes called a reborn fireball (Ghisellini et al. 2007).

The evolution is completely different if the dissipation radius exceeds the photosphere (see §3.5 for other thermalization processes). This is the case (B) in Fig. 3. Relativistic hot motions of protons are not effectively thermalized, which are converted into the bulk motion, leading to a VHLF up to the saturation value $\Gamma_c \sim \eta$ in Eq. (21). Here, the acceleration $\Gamma \propto r$ continues even beyond the photosphere because the pressure is provided by the collisionless hot motions of protons. For a large dissipation radius exceeding the baryonic photosphere $r_m > r_{ph}$, the e^\pm creation is necessary to trap the radiation that boosts the proton energy. Although the e^\pm abundance is somewhat uncertain (see §3.3), we first derive the upper limits on the coasting Lorentz factor by considering the most favorable case. For a dissipation radius $r_m > r_\pm$ in Eq. (26), i.e., in the range $\eta > \eta_{k2}$ where

$$\eta_{k2} = \Gamma_s^{-3/5} \eta_\pm^{8/5} \simeq 1 \times 10^6 \Gamma_s^{-3/5} L_{53}^{2/5} r_{b,8}^{-2/5}, \quad (37)$$

the e^\pm rest mass necessary for trapping the radiation dominates the baryon rest mass, suppressing the coasting Lorentz factor below the saturation value η in Fig. 3. An upper limit to the dissipation radius is $r_m < r_{\pm,\max}$ in Eq. (34), i.e., in the range $\eta < \eta_{k3}$ where

$$\eta_{k3} = \Gamma_s^{-1} \eta_\pm^2 \simeq 4 \times 10^7 \Gamma_s^{-1} L_{53}^{1/2} r_{b,8}^{-1/2}, \quad (38)$$

because the fireball larger than $r_{\pm,\max}$ is too rarefied to trap the radiation even if e^\pm is maximally created. Thus, a dissipated fireball with $\eta > \eta_{k3}$ is never formed via physical processes. Since the e^\pm rest mass equals the total energy at $r_m = r_{\pm,\max}$ in Eq. (34), the dissipated fireball terminates its acceleration.

The final coasting Lorentz factor (red thick line in Fig. 3) may be summarized as

$$\Gamma_c = \begin{cases} \eta & \text{for } \eta < \eta_* \\ \eta_*^{4/3} \eta^{-1/3} & \text{for } \eta_* < \eta < \eta_{k1} \\ \eta & \text{for } \eta_{k1} < \eta < \eta_{k2} \\ \eta_{k2} (\eta/\eta_{k2})^\lambda & \text{for } \eta_{k2} < \eta < \eta_{k3}, \end{cases} \quad (39)$$

where the index λ is determined by the condition $\Gamma_c = r_m/r_b = \sqrt{\Gamma_s \eta_{k3}}$ at $\eta = \eta_{k3}$ (see Fig. 3) as

$$\lambda = -\frac{\ln(\eta_{k2} \Gamma_s^{-1/2} \eta_{k3}^{-1/2})}{\ln(\eta_{k3} \eta_{k2}^{-1})}. \quad (40)$$

TABLE 1
FINAL SHARES OF THE INITIAL TOTAL LUMINOSITY L AS A FUNCTION OF THE RADIATION-TO-BARYON RATIO η . THE LUMINOSITY IS SHARED BY THE PHOTOSPHERIC RADIATION L_{ph} , NEUTRINOS L_ν (SEE §5.1), AND PROTONS AND e^\pm IN THE KINETIC FORM $L_k = L_p + L_\pm$, WHICH IS LATER DISSIPATED VIA INTERNAL/EXTERNAL SHOCKS (SEE §4.1). IN §4.1, WE CONNECT L_{ph} WITH THE BAND SPECTRAL COMPONENT AND L_k WITH THE EXTRA HIGH-ENERGY POWER-LAW COMPONENT (PL IN SHORT), RESPECTIVELY. NOTE THAT THE COASTING LORENTZ FACTOR Γ_c ACHIEVES A VHLF IN THE HIGH ENTROPY RANGE $\eta_{k1} < \eta$ [SEE FIG. 3 AND EQ. (39)]. CRITICAL ENTROPIES η_* , η_{k1} , η_{k2} , AND η_{k3} ARE GIVEN BY EQS. (23), (36), (37), AND (38), RESPECTIVELY.

η	Γ_c	L_{ph} [\sim Band]	L_k [\sim PL]	Spectrum	L_ν
$1 < \eta < \eta_* \sim 10^3$	η	$\ll L$	$\sim L$	PL	$\sim L$
$\eta_* < \eta < \eta_{k1} \sim 10^4$	$\eta_*^{4/3} \eta^{-1/3}$ (or η_*)	$\sim L$	$\ll L$	Band	$\sim L$
$\eta_{k1} < \eta < \eta_{k2} \sim 10^6$	η	$\sim L$	$\sim L_p \sim L$	Band+PL	$\ll L$
$\eta_{k2} < \eta < \eta_{k3} \sim 10^7$	$\eta_{k2}(\eta/\eta_{k2})^\lambda$	$\sim L$	$\sim L_\pm \sim L$	Band+PL	$\ll L$

The appropriate coasting Lorentz factor for $\eta_* < \eta < \eta_{k1}$ would be η_* instead of the slightly smaller $\eta_*^{4/3} \eta^{-1/3}$ in Eq. (39) because most of the electrons above the photosphere can still scatter with a decreasing fraction of free-streaming photons, and continue accelerating as long as the comoving Compton drag time $t'_{\text{drag}} = m_p c^2 / c \sigma_T U'_\gamma$ is less than the comoving dynamical time $t'_{\text{dyn}} = r / c\Gamma$ (Grimsrud & Wasserman 1998; Mészáros & Rees 2000a). The ratio of these two times, $t'_{\text{drag}}/t'_{\text{dyn}} = 4\pi m_p c^3 r \Gamma^3 / L \sigma_T = (r/\eta_* r_b)^4$, gives the coasting radius where the radiative acceleration ceases at $r/r_b = \eta_* > r_{\text{ph}}/r_b$ for $\eta > \eta_*$.

The maximum value of the coasting Lorentz factor is

$$\Gamma_{c,\text{max}} = \eta_{k2} \simeq 1 \times 10^6 \Gamma_s^{-3/5} L_{53}^{2/5} r_{b,8}^{-2/5}, \quad (41)$$

(see Fig. 3), which is a VHLF, much larger than the conventional upper limit $\eta_* \sim 10^3$ in Eqs. (5) and (23). This maximum value is realized by the e^\pm - p equal mass case when the e^\pm rest mass energy is equal to the baryonic one. If the actual e^\pm abundance is less than this case, the radiation escapes without completely transferring its energy to the proton component, leading to a smaller $\Gamma_{c,\text{max}}$. A more conservative estimate of the maximum Lorentz factor is provided by the feasible case of the e^\pm creation in Eq. (33) of §3.3, which gives the feasible optical depth to trap the radiation at the dissipation. By solving $\tau_T = 2n'_\pm \sigma_T r_m / \Gamma_m = 1$ in terms of η , with Eqs. (33), (35), (23), (20), and $n'_p = L/4\pi r_m^2 m_p c^3 \eta \Gamma_m$,

we may identify its solution with the most conservative maximum Lorentz factor as

$$\Gamma_{c,\text{max}} = \left(\frac{16 \sigma_{pp} m_p f_\pm}{3 \sigma_T m_e} \right)^{2/9} \Gamma_s^{-7/9} \eta_*^{16/9} \\ \sim 8 \times 10^5 f_\pm^{2/9} \Gamma_s^{-7/9} L_{53}^{4/9} r_{b,8}^{-4/9}, \quad (42)$$

which is still a VHLF unless f_\pm is very small in Eq. (30). Therefore, we conclude that the coasting Lorentz factor can attain a VHLF, $\Gamma_c \sim 10^4$ – 10^6 , if the dissipation radius is above the photosphere, i.e., in the high entropy range with $\eta > \eta_{k1} \sim 10^4 \Gamma_s^{-3/5}$ (see §3.5 for other thermalization processes). It is interesting to note a sharp rise of Γ_c at $\eta = \eta_{k1}$, where a slight change of the baryon loads could lead to a large difference in the coasting Lorentz factor $\Delta\Gamma_c/\Gamma_c > 10$.

The initial fireball energy is shared by the photospheric radiation luminosity L_{ph} , the neutrino luminosity L_ν (see §5.1), and the kinetic luminosity of protons and e^\pm , $L_k = L_p + L_\pm$, where the kinetic luminosity is later dissipated via internal and external shocks (see §4.1). Table 1 summarizes the final shares of the initial total luminosity L as a function of η . As we discuss in §4.1, if we connect L_{ph} with the Band spectral component and L_k with the extra high-energy power-law component, the equal contributions from both components could suggest the VHLF range with $\eta_{k1} < \eta$ in Table 1, Fig. 3 and Eq. (39), and the GeV onset delay phase could suggest the moderate entropy range $\eta_* < \eta < \eta_{k1}$ (see §4.4).

3.5. Thermalization: pp , $p\gamma$, Coulomb, and plasma processes

We have considered pp collisions for the thermalization process of relativistic protons that are entrained in the fireball dissipation. In this section, we also examine other processes, $p\gamma$ (Bethe-Heitler and photomeson) and Coulomb interactions, which are relevant in some circumstances. (The bremsstrahlung emission is not effective for fiducial parameters.)

The main competing interaction is Bethe-Heitler photopair production ($p\gamma \rightarrow pe^+e^-$). The threshold energy of photons

normalized by the peak energy is about

$$\frac{2m_e c^2 / \gamma'_p}{\varepsilon'_{\text{peak}}} \sim \frac{2m_e c^2}{\varepsilon_{\text{peak}}} 2\Gamma_s \left(\frac{r}{r_m} \right)^2 \sim 3 L_{53}^{-1/2} \Gamma_s \left(\frac{r}{r_m} \right)^2, \quad (43)$$

where $r > r_m$ and we consider the adiabatically cooling protons with the comoving Lorentz factor $\gamma'_p \sim (\Gamma_m/2\Gamma_s)(r_m/r)$ in Eq. (20), photons with energy $\varepsilon'_{\text{peak}} = (r_b/r)\varepsilon_{\text{peak}}$ in Eq. (1), and the dissipation radius $r_m/r_b \sim \Gamma_m$ in Eq. (35). The ratio in Eq. (43) is usually larger than unity. Therefore, the Bethe-Heitler process is not effective for a thermal photon spectrum with a cutoff above the peak energy $\varepsilon_{\text{peak}}$.

Whereas, if the photon spectrum is nonthermal, the protons

can interact with high-energy photons to produce pairs. For a typical Band spectrum, the protons can cool via Bethe-Heitler processes even above the pionosphere without pp collisions. The Lorentz factor of protons decreases to a value γ_p^{BH} for which the Bethe-Heitler cooling optical depth is about unity,

$$n'_\gamma \left(\nu'_\gamma > 2m_e c^2 / \gamma_p^{\text{BH}} \right) K_{\text{BH}} \sigma_{\text{BH}} \frac{r_m}{\Gamma_m} \sim 1, \quad (44)$$

where we estimate at the dissipation radius $r = r_m$ in Eq. (35), and approximate the photon number density above the threshold as

$$n'_\gamma \left(\nu'_\gamma > 2m_e c^2 / \gamma_p^{\text{BH}} \right) = \frac{\left(2m_e c^2 / \gamma_p^{\text{BH}} \varepsilon'_{\text{peak}} \right)^{1-\beta} L}{4\pi r_m^2 c \Gamma_m^2 \varepsilon'_{\text{peak}} (\beta-1)}, \quad (45)$$

with the high-energy photon index $\beta \sim 2.5$, the cross section $\sigma_{\text{BH}} \sim (e^2/\hbar c)(3/8\pi)\sigma_T$ and the inelasticity $K_{\text{BH}} \sim m_e/m_p$ for the Bethe-Heitler process. We note that the value $K_{\text{BH}}\sigma_{\text{BH}} \sim 5 \times 10^{-31} \text{ cm}^2$ changes by less than a factor of 3.5 for the range $5 \leq \nu'_\gamma \gamma'_p / m_e c^2 \leq 10^3$ (Chodorowski et al. 1992). From Eqs. (44) and (45), we obtain the Lorentz factor of protons after the Bethe-Heitler cooling as

$$\gamma_p^{\text{BH}} \sim \frac{2m_e c^2 \Gamma_m}{\varepsilon_{\text{peak}}} \left[\Gamma_s^{3/2} \eta^{3/2} \eta_*^{-4} \frac{\varepsilon_{\text{peak}}}{m_p c^2} \frac{\sigma_T (\beta-1)}{K_{\text{BH}} \sigma_{\text{BH}}} \right]^{1/(\beta-1)} \quad (46)$$

with Eqs. (23) and (35) and $\Gamma_m \varepsilon'_{\text{peak}} = \varepsilon_{\text{peak}}$, where γ_p^{BH} does not drop to unity in most cases, differently from the pp collisional case. We can neglect the Bethe-Heitler cooling above the dissipation radius as the number density of photons above the threshold rapidly decreases as $n'_\gamma(\nu'_\gamma > 2m_e c^2 / \gamma_p^{\text{BH}}) \propto r^{-(2\beta+1)}$. The leftover relativistic motions of protons in Eq. (46) are converted into the bulk motion via collisionless bulk acceleration. Therefore, in the case of the effective Bethe-Heitler cooling, we derive the final coasting Lorentz factor as

$$\frac{\Gamma_c^{\text{BH}}}{\eta} = \frac{\Gamma_m \gamma_p^{\text{BH}}}{\eta} = \left(\frac{\eta}{\eta_{\text{BH}}} \right)^{3/2(\beta-1)}, \quad (47)$$

where

$$\eta_{\text{BH}} = \Gamma_s^{-(2\beta+1)/3} \eta_*^{8/3} \left(\frac{\varepsilon_{\text{peak}}}{2m_e c^2} \right)^{2(\beta-1)/3} \left[\frac{m_p c^2}{\varepsilon_{\text{peak}}} \frac{K_{\text{BH}} \sigma_{\text{BH}}}{\sigma_T (\beta-1)} \right]^{2/3} \\ \sim 6 \times 10^5 \Gamma_s^{-(2\beta+1)/3} L_{53}^{2/3} r_{b,8}^{-2/3} \varepsilon_{\text{peak,MeV}}^{2(\beta-2)/3}, \quad (48)$$

with Eq. (23). In Fig. 3, we plot Γ_c^{BH} of Eqs. (47) and (48). We can see that the Bethe-Heitler process can reduce the proton kinetic energy by $\sim \Gamma_c^{\text{BH}}/\Gamma_c \sim \Gamma_c^{\text{BH}}/\eta \sim 0.03$ –1 times (at most) in the range of the dimensionless entropy $\eta_{k1} < \eta < \eta_{\text{BH}}$. Nevertheless, the coasting Lorentz factor can attain a VHLF even if the Bethe-Heitler cooling is most effective. The actual evolution would be between Γ_c and Γ_c^{BH} in Fig. 3, but is difficult to evaluate exactly since it depends on the photon spectrum below the photosphere, which could be thermal or could already be the Band spectrum (see §5.2). We also note that the coasting Lorentz factor could be larger than Γ_c^{BH} if the e^\pm pairs produced by the Bethe-Heitler process make a photosphere above the coasting radius since the radiative acceleration continues up to the photospheric radius.

The other photoprocess is the photomeson interaction, which produces one or more mesons, mostly pions. The

threshold is higher by $m_\pi/m_e \sim 280$, while the mean cross section $K_{pm}\sigma_{pm} \sim 7 \times 10^{-29} \text{ cm}^2$ is ~ 140 times higher than the Bethe-Heitler process (Chodorowski et al. 1992). Then, the ratio of the photomeson cooling to the Bethe-Heitler cooling is

$$\frac{K_{pm}\sigma_{pm}}{K_{\text{BH}}\sigma_{\text{BH}}} \left(\frac{m_\pi}{m_e} \right)^{1-\beta} \sim 3 \times 10^{-2} \quad \text{for } \beta = 2.5, \quad (49)$$

and ~ 0.5 for $\beta = 2$. Thus, the photomeson cooling is subdominant for a typical Band spectrum with $\beta > 2$.

The Coulomb collisions with e^\pm also contribute to the proton cooling because the temperature of e^\pm is usually kept at a nonrelativistic value, much below the proton temperature, by the Compton cooling (Beloborodov 2009). The effective radius of the Coulomb cooling is determined by

$$n'_\pm \frac{r}{\Gamma} \frac{m_e}{m_p} \sigma_T \ln \Lambda \sim 1, \quad (50)$$

where $\ln \Lambda \sim 10$ is the Coulomb logarithm. That is, the Coulomb cooling is effective if the Thompson optical depth is larger than $\tau_T > m_p/m_e \ln \Lambda \sim 200$. Assuming the feasible e^\pm density in Eq. (33) at the dissipation radius r_m in Eq. (35), we can estimate the range of the dimensionless entropy η where the Coulomb collisions are effective as

$$\eta < \eta_C \equiv \eta_*^{16/9} \Gamma_s^{-7/9} \left[\frac{4}{3} \frac{\sigma_{pp}}{\sigma_T} \frac{m_e}{m_p} f_\pm (\ln \Lambda)^2 \right]^{2/9} \\ \sim 6 \times 10^4 L_{53}^{4/9} r_{b,8}^{-4/9} \Gamma_s^{-7/9} f_\pm^{2/9}, \quad (51)$$

with Eq. (20) and the relation $n'_p = L/4\pi r_m^2 m_p c^3 \eta \Gamma_m$. Then, for the maximum e^\pm multiplicity $f_\pm \sim 0.5$ in Eq. (30), we have $\eta_C > \eta_{k1} \sim 2 \times 10^4$ in Eq. (36) and Fig. 3, that is, the protons cool via Coulomb collisions for $\eta_{k1} < \eta < \eta_C$ even above the pionosphere without pp collisions. (Note that the pp collisions dominate the Coulomb collisions for $\eta \lesssim \eta_{k1}$ even in this case). The random Lorentz factor of the protons decreases, reducing the collisionless pressure, although it may not completely vanish since the e^\pm density also decreases as the protons, i.e., the energy source of e^\pm , cool down. Then, the coasting Lorentz factor Γ_c for $\eta_{k1} < \eta < \eta_C$ could not attain the saturation value $\Gamma_c = \eta$ in Eq. (39) and Fig. 3. Nevertheless, the ratio $\eta_C/\eta_{k1} \sim 3$ is just a factor and does not depend on the parameters so much ($\eta_C/\eta_{k1} \propto L^{2/45} r_b^{-2/45} \Gamma_s^{-1/5}$). Thus, the critical entropy η_{k1} for the pp collisions in Eq. (36) is still a good indicator of the VHLF fireball formation.

In addition to the above two-body processes, the collective plasma processes could dissipate the relativistic proton energy. At least, a fraction ($\epsilon_B \sim 0.01$) of the proton energy could be converted into the magnetic field via the Weibel instability (Medvedev & Loeb 1999) or the macroscopic turbulence (Goodman & MacFadyen 2008; Sironi & Goodman 2007; Zhang et al. 2009). However, the conversion into the magnetic field does not reduce the coasting Lorentz factor because the magnetic field also provides the relativistic pressure to expand the fireball (see §3.7). Rather, it opens up a way to the VHLF since the magnetic pressure can persist even after the proton cooling via two-body processes. On the other hand, the dissipation of the proton energy into electrons is harmful for making the VHLF. However, the energy conversion fraction is usually less than half ($\epsilon_e < 0.5$) (Spitkovsky 2008; Toma et al. 2008). The plasma dissipation would be also suppressed after the protons are isotropized. Therefore,

the plasma processes are unlikely obstacles to the VHLF formation.

3.6. Consistency with previous works

We have discussed a physical mechanism of the collisionless bulk acceleration to create VHLF fireballs with $\Gamma_c > \eta_* \sim 10^3$ up to $\Gamma_c \lesssim 10^6$ in the previous sections. Since such a VHLF is somewhat extreme and has not been considered seriously, we examine whether a VHLF is allowed by the previous observations.

(1) A high-energy cutoff due to e^\pm creation provides information on the bulk Lorentz factor of a fireball (Baring & Harding 1997; Lithwick & Sari 2001; Razzaque et al. 2004; Murase & Ioka 2008; Aoi et al. 2009). This method usually gives a lower limit on the bulk Lorentz factor, which is about $\Gamma_c > 10^2$ – 10^3 so far (Abdo et al. 2009b,a, 2010c) and consistent with a VHLF (see §4.3 for GRB 090926). Further observations are needed, and hopefully, more elaborate observations are necessary because the exponential cutoff is usually smoothed to a broken power-law by multizone effects, which make it difficult to identify the cutoff (Aoi et al. 2009; Li 2010a; Granot et al. 2008; Bosnjak et al. 2009).

(2) For the internal shocks to take place before the external shock, the minimum Lorentz factor in the flow has to be below $\Gamma \lesssim 3 \times 10^4$. (Rees & Mészáros 1994; Sari & Piran 1997a) This is because the internal shock radius becomes larger for higher Γ ,

$$r_{\text{sh}} = 2\Gamma^2 ct_v \sim 6 \times 10^{15} \text{ cm } \Gamma_{4t_{v,-3}}^2. \quad (52)$$

On the other hand, the afterglow starts when the reverse shock crosses the shell. Since a VHLF evolution is in the so-called thick shell case, the reverse shock crosses at the duration time T . After that, the hydrodynamic evolution enters into the self-similar phase, which may be described by the adiabatic condition $E \sim (4\pi/3)\gamma^2 r^3 n m_p c^2$. Eliminating γ with $T \sim r_{\text{ex}}/4\Gamma^2 c$, we obtain the reverse shock crossing radius as

$$r_{\text{ex}} \sim 7 \times 10^{16} \text{ cm } E_{53}^{1/4} n^{-1/4} T_1^{1/4}, \quad (53)$$

which do not depend on Γ . We note that a VHLF with $\Gamma \gtrsim 3 \times 10^4$ is allowed if it is decelerated by internal shocks with slower shells before external shocks. This is even favorable for efficient internal shocks (Kobayashi et al. 1997; Kobayashi & Sari 2001; Beloborodov 2000), and also for the GeV onset delay in §4.4

(3) By identifying the peak time of the afterglow light curve with the decelerating time of the ejecta, we can constrain the Lorentz factor (Sari & Piran 1999b; Rykoff et al. 2009; Ghirlanda et al. 2010; Liang et al. 2009). Several results do not imply VHLF values but typically $\Gamma \sim 100$ – 600 . However, this method is only applicable to the so-called thin shell case, whereas a VHLF evolution is likely a thick shell case. In the thin shell case, the peak time of the afterglow light curve is expected to be later than the prompt emission, while in the thick shell case, the peak time is comparable to the prompt duration and difficult to observe. This method also gives a lower limit on the Lorentz factor if the flow is decelerated by internal shocks with slower shells before external shocks.

(4) Reverse and forward shock emission in the early afterglows constrains the Lorentz factor via spectral and temporal modelings (Sari & Piran 1999a; Zhang et al. 2003). Several results do not imply the VHLF. However, the early afterglow modelings are confronted with difficulties to interpret

the steep and shallow decay discovered by *Swift* (see also §5.6) (Zhang et al. 2006; Ioka et al. 2006; Panaitescu et al. 2006; Zhang et al. 2006; Huang et al. 2006; Sato et al. 2007). This method also gives a lower limit on the Lorentz factor if the flow is decelerated by internal shocks with slower shells before external shocks.

(5) We can infer the Lorentz factor by identifying the spectral peak $L(\nu = \varepsilon_{\text{peak}})$ with the thermal emission component (Pe’er et al. 2007; Ryde et al. 2010). Pe’er et al. and Ryde et al. applied this method to several bursts including GRB 090902B and suggested $\Gamma \sim 300$ – 800 below a VHLF. However, this method potentially has two solutions, one of which may provide a low Lorentz factor, whereas the other could be the real case with a VHLF. To be more precise, this method initially discriminates two possible cases, $r_{\text{ph}} > r_s$ and $r_{\text{ph}} < r_s$, where it is possible to determine the Lorentz factor only in the case of $r_{\text{ph}} > r_s$. This case also provides a consistency inequality ($\eta < \eta_*$) between observables, so one might think that this is the solution if the inequality is satisfied. However, it is logically not a sufficient condition but just a necessary condition to satisfy the inequality, so that we cannot exclude the other case $r_{\text{ph}} < r_s$, which allows a VHLF.

(6) Zhang and Pe’er (Zhang & Pe’er 2009; Fan 2010) claim that the predicted thermal component is not consistent with the observation, suggesting that the outflow is not radiation-dominated but Poynting-dominated. They estimate the maximum temperature allowed by the observation of GRB 080916C as $T_{\text{ph,max}}^{\text{ob}} = 50$ keV, using the relation $r_b = c\delta t^{\text{ob}}$ with the observed variability time $\delta t^{\text{ob}} = 0.5$ s, and conclude that this is below and contradicts with the observed peak energy. However, the central engine size may be smaller than $c\delta t^{\text{ob}}$, so that we can raise the maximum temperature with $T_{\text{ph,max}} \propto r^{-1/2}$ to fit the observation. In addition, the photosphere model usually assumes that the black body spectrum is modified to a Band spectrum by Comptonization via magnetic reconnection, neutron collisions or repeated shocks, (Thompson et al. 2007; Mészáros & Rees 2000a; Ioka et al. 2007; Beloborodov 2009; Giannios & Spruit 2007; Giannios 2008) although the actual mechanism has not yet been revealed (see also §5.2) (Ioka et al. 2007). Then, it is possible to reproduce the observed spectrum by the photospheric emission.

(7) Zou and Piran (Zou & Piran 2010) gave an upper limit on the Lorentz factor by requiring that the observed deep minimum in the prompt phase should be above the early external shock emission. The results are $\Gamma \lesssim 10^3$, not a VHLF. Since they present an analysis only for the thin shell case, it is desirable to calculate the thick shell case, which is the likely case for the VHLF evolution. This method also gives a lower limit on the Lorentz factor if the flow is decelerated by internal shocks with slower shells before external shocks.

In conclusion, the VHLF fireballs are currently consistent with previous observations.

3.7. Connection with magnetic acceleration

A VHLF can also be achieved by the magnetic acceleration of a fireball. If the energy density is dominated by the magnetic fields, the magnetic pressure expands the fireball up to the equipartition of the comoving energy density between the magnetic fields and matter (protons and/or electrons) (Mészáros & Rees 1997).

The difference between the magnetic acceleration and the collisionless bulk acceleration is in the radiation fraction

L_{ph}/L after the evolution. In the collisionless bulk acceleration, the radiation fraction L_{ph}/L is about unity for the VHFLF fireballs in Table 1. Whereas, in the magnetic acceleration, the radiation fraction L_{ph}/L depends on the initial condition (i.e., the radiation and e^{\pm} fraction) and the magnetic reconnection during the expansion, thereby not determined from the first principle.

We can also consider the magnetic component in the collisionless bulk acceleration. Firstly, the magnetic field could be advected from the central engine. In this case, the final radiation fraction L_{ph}/L becomes less than unity because the magnetic component occupies a fraction of the final luminosity as a nonradiative component. The magnetic component from the central engine could be relevant for the short GRBs as discussed in §5.7. Secondly, the magnetic field could be generated by the relativistic proton component via plasma processes at the fireball dissipation (see §3.5). This does not reduce the final radiation fraction L_{ph}/L . The magnetic pressure could persist even after the proton cooling, expanding a way to the VHFLF.

4. FIREBALL SPECTRUM: HOT PHOTOSPHERE–INTERNAL–EXTERNAL SHOCK SYNCHROTRON MODEL

In this section, we apply VHFLF fireballs to the GRB emission. In §4.1, we first discuss the GRB emission site from the kinematical point of view without detailed spectral modelings. In §4.2, we calculate the internal shock synchrotron spectrum and find that the VHFLF models have advantages on providing a single rising power-law spectrum over >7 energy digits and also the high internal shock efficiency to supply sufficient energy to the power-law component that is comparable to the Band component. In §4.3, we discuss the possible origins of the spectral break at approximately 1.4 GeV observed in the extra component of GRB 090926, which was suggested as the e^{\pm} creation cutoff for $\Gamma \sim 600$. In the VHFLF models, the spectral break could be the synchrotron cooling break for $\Gamma \sim 10^4$, or the maximum synchrotron cutoff, particularly limited by the dynamical time, for $\Gamma \sim 10^5$. In §4.4, we suggest that the GeV onset delay reflects the timescale for the baryon loading rate to change at the dissipation radius, i.e., the environmental change around the progenitor star controls the GeV onset delay. We can predict the delay time and also its parameter dependences, which are found to be consistent with the observations.

4.1. Emission sites

The GRB emission has at least two, and probably three components: (1) the usual Band component (a broken power-law with a peak at $\varepsilon_{\text{peak}} \sim 0.1\text{--}1$ MeV), (2a) high-energy emission (> 100 MeV) that lasts longer than the MeV emission, (Hurley et al. 1994; González et al. 2003) showing a power-law decay, as revealed by Fermi/LAT (Abdo et al. 2009c,a,b, 2010b,c), (2b) high-energy variable emission (> 100 MeV) that looks correlated with the MeV emission with a short rise and decay time scale (Abdo et al. 2009a). Most of the spectra are well fitted by the Band function even up to ~ 10 GeV, while an additional distinct component at $\gtrsim 10$ MeV is also found, at least in GRB 090510 and 090902B out of ~ 12 Fermi/LAT bursts. This additional component is fitted by a single power-law that slightly rises in $\nu F_{\nu} \propto \nu^{0.1\text{--}\nu^{0.4}}$ and often extends below $\lesssim 20$ keV over ~ 7 energy digits. (However, note that no other experiments have confirmed the low-energy extension of the power-law component.)

Figure 4 shows our model in a schematic way. This is essentially the same as the photosphere–internal shock model proposed by Toma et al. (Toma et al. 2010) (see §4.2 for differences in the Lorentz factor and hence the emission mechanism). In this model, we consider the following emission site for each emission component,

- (1) Band component: Photospheric emission,
- (2a) Long-lived power-law component: External shock,
- (2b) Variable power-law component: Internal shock.

These assignments seem reasonable from the kinematical point of view, even without detailed spectral modelings, because of the following reasons:

- A photospheric origin of the Band component easily explains the high radiative efficiency, in addition to the low-energy spectral index and the stability of the spectral $\varepsilon_{\text{peak}}$ relation (see §1). The radiative efficiency (i.e., the ratio of the photospheric luminosity L_{ph} to the total luminosity L) can be more than $\sim 50\%$ if the radiation to baryon ratio is in the moderate to high entropy range $\eta > \eta_* \sim 10^3$, as summarized in Table 1 with Eq. (23). The dissipation under the photosphere is suggested by the $\varepsilon_{\text{peak}}\text{--}L$ Yonetoku relation (see §3.1).
- An external shock origin of the long-lived power-law component has an advantage for explaining its longevity and power-law decay. The high-energy long-lived emission could be consistent with the simple synchrotron emission from the external forward shock, with either adiabatic (Kumar & Barniol Duran 2009a,b; Barniol Duran & Kumar 2010; Corsi et al. 2009a,b; Gao et al. 2009; De Pasquale et al. 2010; Pandey et al. 2010) or radiative shock (Ghirlanda et al. 2010; Ghisellini et al. 2010) and probably the Klein-Nishina effect (Wang et al. 2010; Nakar et al. 2009). Although the maximum synchrotron frequency has not been detected (Li 2010b; Piran & Nakar 2010), the long-lived component could be produced by the inverse Compton emission (Zou et al. 2009; Wang et al. 2010; Corsi et al. 2009a; Neamus 2010; Murase et al. 2010). As we can see from Table 1, the kinetic energy of the external shock is comparable to the total energy if $\eta > \eta_{k1} \sim 10^4 \Gamma_s^{-3/5}$ in the VHFLF range and $\eta < \eta_* \sim 10^3$ in the low entropy range with Eqs. (23) and (36).
- An internal shock origin is naturally invoked for the variable high-energy component because the external shock cannot usually produce fast variability (Sari & Piran 1997b; Ioka et al. 2005). The external shocks cannot have the fast decay of the light curve (Ioka et al. 2005), although the fast rise could be produced by the finite acceleration time of particles that radiate at the observed energy (Barniol Duran & Kumar 2010). It is favorable to have VHFLF fireballs in addition to slow ones, i.e., a large dispersion in the Lorentz factor, to raise the internal shock efficiency for converting the kinetic energy into radiation (Kobayashi et al. 1997; Kobayashi & Sari 2001; Beloborodov 2000), because the variable power-law component has a comparable luminosity to the Band component in several bursts. It is interesting to note a sharp rise of the coasting Lorentz

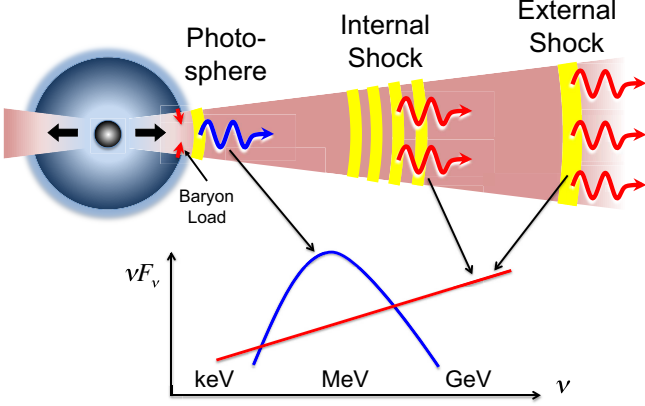


FIG. 4.— Photosphere–internal–external shock model (Toma et al. 2010) in which the photospheric emission produces the Band spectrum, the internal shock contributes the variable power-law spectrum, and the external shock makes the long-lived power-law spectrum. The central core of a massive star or the merged compact star gravitationally collapses into a black hole or neutron star, which somehow launches a collimated jet. Dissipation via shocks internally or with nearby matter under the photosphere determines the baryon loads and subsequent fireball evolution, where low baryon loads lead to a VHLF, as in Fig. 3 and Table 1.

factor Γ_c at $\eta = \eta_{k1} \sim 10^4 \Gamma_s^{-3/5}$ in Fig. 3, where a slight change in the baryon loads leads to a large difference in the Lorentz factor $\Delta\Gamma_c/\Gamma_c > 10$.

We note that the bulk Compton emission is another possibility to produce the extra GeV component in the VHLF models. Since the emission depends on the ambient photon fields, we leave it as a future work.

4.2. GeV spectrum: internal shock synchrotron model

A VHLF could be a key for internal shocks to make the variable power-law spectrum that is slightly rising as $\nu F_\nu \propto \nu^{0.1-0.4}$, sometimes over ~ 7 energy digits from $\gtrsim 10$ GeV down to $\lesssim 20$ keV. In the following, we propose the simple internal shock synchrotron model with a VHLF for the extra spectral component.

The internal shocks convert the kinetic energy into internal energy with the energy density of

$$U' = \frac{L}{4\pi r_{\text{sh}}^2 c \Gamma^2} = \frac{L}{16\pi c^3 t_v^2 \Gamma^6}, \quad (54)$$

where the shock at a radius $r_{\text{sh}} = 2c\Gamma^2 t_v$ makes a variability of time t_v . We assume that electrons are accelerated in the internal shock to a power-law distribution of Lorentz factor γ'_e , $dn'_e/d\gamma'_e \propto \gamma_e^{-p}$ for $\gamma'_e \geq \gamma'_m$ and $p > 2$. As we have discussed in §§3.3 and 3.5, abundant e^\pm pairs likely exist. We parametrize the e^\pm number density as

$$n'_e = \mathcal{R}n'_p = \mathcal{R} \frac{U'}{\bar{\gamma}' m_p c^2}, \quad (55)$$

where $\bar{\gamma}'$ is the random Lorentz factor of protons. If a fraction of internal energy goes into the electron acceleration, $U'_e = \epsilon_e U'$, the minimum electron Lorentz factor is given by

$$\gamma'_m = \epsilon_e \frac{p-2}{p-1} \frac{m_p}{m_e} \frac{\bar{\gamma}'}{\mathcal{R}} \sim 300 \epsilon_e \bar{\gamma}' \mathcal{R}^{-1} f_p, \quad (56)$$

where $f_p = 6(p-2)/(p-1)$. We further assume that a fraction of internal energy goes into the magnetic field amplification,

$$B' = (8\pi\epsilon_B U')^{1/2} \sim 4 \text{ G} \Gamma_4^{-3} L_{53}^{1/2} \epsilon_{B,-2}^{1/2} t_{v,-3}^{-1}. \quad (57)$$

Thus, the electron synchrotron cooling is effective above

$$\gamma'_c = \frac{6\pi m_e c}{\sigma_T B'^2 \Gamma t_v} \sim 4 \times 10^6 \Gamma_4^5 L_{53}^{-1} t_{v,-3} \epsilon_{B,-2}^{-1}. \quad (58)$$

With the synchrotron formula $\nu(\gamma'_e) = 3q_e B' \Gamma \gamma_e'^2 / 4\pi m_e c$, we have the synchrotron characteristic and cooling frequencies as

$$\nu_m = 50 \text{ eV} \Gamma_4^{-2} L_{53}^{1/2} t_{v,-3}^{-1} \epsilon_e^2 \epsilon_{B,-2}^{1/2} \bar{\gamma}'^2 \mathcal{R}^{-2} f_p^2, \quad (59)$$

$$\nu_c = 9 \text{ GeV} \Gamma_4^8 L_{53}^{-3/2} t_{v,-3} \epsilon_{B,-2}^{-3/2}, \quad (60)$$

respectively. Because of the slow cooling $\nu_m < \nu_c$ for a VHLF, the spectrum is

$$\nu F_\nu^{\text{syn}} \propto \begin{cases} \nu^{4/3}, & \nu < \nu_m \\ \nu^{(3-p)/2}, & \nu_m < \nu < \nu_c \\ \nu^{(2-p)/2}, & \nu_c < \nu, \end{cases} \quad (61)$$

where the synchrotron luminosity at $\nu = \nu_c$ is about

$$\frac{L_{\text{syn}}(\nu_c)}{L} = \epsilon_e \left(\frac{\gamma'_m}{\gamma'_c} \right)^{p-2} = \epsilon_e \left(\frac{\nu_m}{\nu_c} \right)^{(p-2)/2}, \quad (62)$$

since electrons above γ'_c cool effectively.

Figure 5 shows the internal shock synchrotron spectrum with a VHLF, $\Gamma = 10^4$, for fiducial parameters, $L = 10^{53}$ erg s^{-1} , $\epsilon_e = 1$, $\epsilon_B = 10^{-2}$, $t_v = 10^{-3}$ s, $\mathcal{R} = 10$, $\bar{\gamma}' = 10$, $p = 2.2$, and redshift $z = 1$. Here, the attenuation by the e^\pm creation with the cosmic infrared background becomes important at $\gtrsim 20$ GeV, which is taken into account using the best-fit model of Kneiske et al. (2004) (Kneiske et al. 2004).

From Fig. 5, we can find that the VHLF internal shock synchrotron model has the following advantages.

- (1) First, the extra component has a single rising power-law spectrum over many energy digits. Thanks to the strong dependence of ν_c on the Lorentz factor, $\nu_c \propto \Gamma^8$, a VHLF internal shock has a high cooling frequency ν_c beyond $\nu_c \gtrsim 10$ GeV. The Γ dependence is $\nu_m \propto \Gamma^{-2}$ for the characteristic frequency ν_m , extending a power-law below < 1 keV. In combination, the rising segment of the $\nu F_\nu \propto \nu^{(3-p)/2}$ spectrum is stretched to

$$\frac{\nu_c}{\nu_m} \sim 2 \times 10^8 \left(\frac{\Gamma}{10^4} \right)^{10} \quad (63)$$

for fiducial parameters with Eqs. (59) and (60). Therefore, a VHLF could be crucial for making a single power-law spectrum that is rising over >7 energy digits.

- (2) Second, the VHLF models may have the high internal shock efficiency, which can supply sufficient energy to the extra component that is comparable to the photospheric Band component. From Eq. (62), the luminosity of the high-energy component is almost equal to the photospheric one, $L_{\text{syn}}(\nu_c) \sim L_{\text{ph}} \sim L$, if $p \approx 2$ and $\epsilon_e \approx 1$. The high-electron-energy fraction $\epsilon_e \approx 1$ may be realized by highly efficient internal shocks between VHLF and slow shells, and also by e^\pm -rich shells expected for fireballs after dissipation (see §§3.3 and 3.5).

Alternatively, the power-law spectrum may be shaped by the superposition of emission from continuous regions and/or

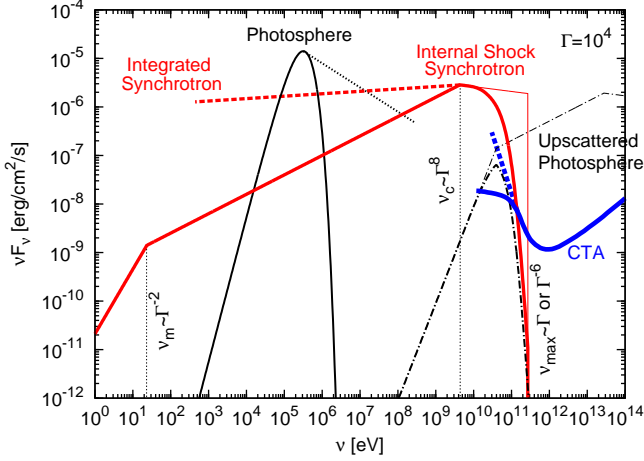


FIG. 5.— Spectrum for the internal shock synchrotron model with a VHLF $\Gamma = 10^4$, for fiducial parameters, $L = 10^{53}$ erg s $^{-1}$, $\epsilon_e = 1$, $\epsilon_B = 10^{-2}$, $t_v = 10^{-3}$ s, $\mathcal{R} = 10$, $\bar{\gamma}' = 10$, $p = 2.2$, and redshift $z = 1$, with (thick solid line) and without (thin solid line) the attenuation by the cosmic infrared background (Kneiske et al. 2004). Thanks to the dependences on the Lorentz factor of the cooling frequency $\nu_c \propto \Gamma^8$ and of the characteristic synchrotron frequency $\nu_m \propto \Gamma^{-2}$, the rising segment of the $\nu F_\nu \propto \nu^{(3-p)/2}$ spectrum is stretched over > 7 energy digits. The maximum synchrotron cutoff is determined by the cooling time $\nu_{\max}^{\text{cool}} \propto \Gamma$ in Eq. (72) or by the dynamical time $\nu_{\max}^{\text{dyn}} \propto \Gamma^{-6}$ in Eq. (73), which could produce the \sim GeV cutoff as observed in GRB 090926 for a VHLF case, $\Gamma \sim 10^4 - 10^5$. The spectral integration over continuous regions and/or times would lead to a flat spectrum in Eq. (64) (dashed line). We also show the photospheric spectrum (solid line) with a Comptonized component (dotted line), and the upscattered photospheric spectrum with (thick dot-dashed line) and without (thin dot-dashed line) the attenuation. These are compared with the CTA sensitivity where we raise the public one by (50 hr/10 s) for simplicity (as the worst case). The actual sensitivity in low energy could be worse than the public one (Teshima 2010).

times. Since the dependence of the cooling frequency ν_c on the Lorentz factor Γ is strong, a slight change in Γ results in a large shift of ν_c , and hence, in a relatively flat νF_ν spectrum. As an example, we assume $L \propto \Gamma^\lambda$ and $\bar{\gamma} \propto \Gamma^{1/2}$ for simplicity. Then, with $\nu_c \propto \Gamma^8 L^{-3/2}$ and $L_{\text{syn}}(\nu_c) \propto L(L\bar{\gamma}\Gamma^{-5})^{p-2}$ in Eqs. (59), (60), and (62), the envelope of the spectrum integrated over continuous regions and/or times becomes relatively flat as

$$\Sigma(\nu F_\nu^{\text{syn}}) \propto \nu^{\frac{2\lambda + (\lambda - 9)(p-2)}{16-3\lambda}} \sim \nu^{0.05} \quad \text{for } \nu < \nu_c, \quad (64)$$

where the last equality is for $p = 2.2$, and $\lambda = 1$, i.e., the case when the luminosity is proportional to the kinetic energy, which may be reasonable.

Our model predicts a temporal correlation between the extra power-law component in the low (\sim keV)-energy region and the high (\sim GeV)-energy region, because a single emission mechanism produces the whole power-law component. In the integrated synchrotron case in Eq. (64), the low-energy component could be delayed by the variability time, i.e., the dynamical time for the Lorentz factor to change. The photospheric Band component is also expected to be temporally correlated with the power-law component, at least within the variability time, because the photospheric luminosity is comparable to the kinetic one for the VHLF range, as shown in Table 1, and the internal shock emission is delayed by the variability time at most.

Toma et al. (2010) (Toma et al. 2010) showed that the photospheric emission can be efficiently scattered by the electrons in the internal shocks, and the Compton upscattered photospheric emission can explain the observed distinct high-

energy component. The low-energy part of the power-law emission at $\lesssim 20$ keV is attributed to the synchrotron emission, i.e., a different origin from the high-energy part. This is different from the VHLF models that employ only a single emission mechanism (synchrotron emission) and may be favorable for explaining a single power-law component over > 7 energy digits. In the VHLF models, the upscattered emission is beyond the Fermi energy range, because the characteristic frequency of upscattered photons is $\sim \gamma_m^2 m_e \epsilon_{\text{peak}} > 1$ TeV (see Fig. 5), which is rather a nice target for the future Cherenkov Telescope Array (CTA) Project. The electron cooling by the Compton upscattering is also suppressed by the Klein-Nishina effect. The emissivity ratio of the upscattered photosphere to the synchrotron is

$$Y_{\text{up}}(\gamma'_e) = \frac{P_{\text{up}}(\gamma'_e)}{P_{\text{syn}}(\gamma'_e)} \simeq \frac{U'_{\text{ph}}[\nu < \nu_{\text{KN}}(\gamma'_e)]}{U'_B}, \quad (65)$$

where $\nu_{\text{KN}}(\gamma'_e) = \Gamma_{\text{sh}} m_e c^2 / \gamma'_e$ and the step function approximation in the second equality is appropriate if $d \ln U'_{\text{ph}} / d \ln \nu < 2$ for $\nu > \nu_{\text{KN}}$ (Wang et al. 2010; Nakar et al. 2009). Since the comoving energy density of photospheric photons is approximated by

$$U'_{\text{ph}}[\nu < \nu_{\text{KN}}(\gamma'_e)] \simeq U' \left[\frac{\nu_{\text{KN}}(\gamma'_e)}{\epsilon_{\text{peak}}} \right]^{2-\alpha}, \quad (66)$$

for $\nu_{\text{KN}} < \epsilon_{\text{peak}}$, the upscattering dominates the synchrotron in the electron cooling $Y_{\text{up}}(\gamma'_e) > 1$ at $\gamma'_e < \gamma'_Y$ where

$$\gamma'_Y \sim \frac{\Gamma m_e c^2}{\epsilon_{\text{peak}}} \epsilon_B^{-1/(2-\alpha)} \sim 5 \times 10^5 \Gamma_4 \epsilon_{\text{peak, MeV}}^{-1/(2-\alpha)} \epsilon_{B,-2}^{-1/(2-\alpha)} \quad (67)$$

for $\alpha = 1$. This is lower than γ_c in Eq. (58), and hence, the electrons mainly cool via synchrotron, not via the inverse Compton, for the VHLF models. (Note that we have to take the Compton cooling into account when we precisely calculate the low-energy end of the integrated spectrum in Eq. (64), which is produced by the decelerated shocks.) We can also neglect the SSC emission (Pilla & Loeb 1998; Sari & Esin 2001; Fan et al. 2008; Zou et al. 2009; Nakar et al. 2009; Wang et al. 2010), since the synchrotron photon density is lower and the peak energy is higher than those of the photospheric emission.

The synchrotron component could also be detected in the optical band. It could explain the bright optical prompt emission in some GRBs, which is brighter than the extrapolation of the Band component (Yost et al. 2007; Racusin et al. 2008).

4.3. GRB 090926: e^\pm creation cutoff, cooling break or maximum synchrotron cutoff?

Recently, a spectral break at approximately 1.4 GeV has been found in the extra power-law component of GRB 090926. We consider the possible origins of the break in the following.

(1) The $\gamma\gamma$ annihilation with e^\pm creation leads to a spectral break (Baring & Harding 1997; Lithwick & Sari 2001; Razzaque et al. 2004; Murase & Ioka 2008; Aoi et al. 2009) at

$$\nu_{\gamma\gamma} \sim 20 \text{ GeV} \left[\xi_{-1}^{-1} L_{53}^{-1} \Gamma_3^{2+2\beta} t_{v,-3} \epsilon_{\text{peak, MeV}}^{2-\beta} (\beta - 1) \right]^{\frac{1}{\beta-1}}, \quad (68)$$

which is determined by the optical depth condition $\tau(\nu) \sim \xi(\beta) n'_\gamma(\nu'_\gamma > \tilde{\nu}') \sigma_T r_{\text{sh}} / 2\Gamma = 1$, where $\tilde{\nu}' = m_e^2 c^4 / \nu'$,

$\xi(\beta) \simeq 7(\beta - 1)/[6\beta^{5/3}(\beta + 1)] \sim 0.1$, (Svensson 1987; Murase & Ioka 2008) and we approximate the photon number density as

$$n'_\gamma(\nu'_\gamma > \tilde{\nu}') = \frac{(\tilde{\nu}'/\varepsilon'_{\text{peak}})^{1-\beta} L}{4\pi r_{\text{sh}}^2 c \Gamma^2 \varepsilon'_{\text{peak}} (\beta - 1)}, \quad (69)$$

with $\beta = 2.5$. Thus, the break at ~ 1.4 GeV suggests the bulk Lorentz factor of ~ 600 . This constraint is applicable to the outermost shell, not excluding VHLF shells behind the slower shell. (Note that this alignment is even preferred by the considerations of the GeV onset delay in §4.4). The e^\pm creation cutoff disappears if $\tilde{\nu}'_{\gamma\gamma} < \varepsilon_{\text{peak}}$, that is,

$$\Gamma > \Gamma_{\gamma\gamma} = \left[\frac{\xi(\beta)L\sigma_T}{16\pi c^2 t_v \varepsilon_{\text{peak}} (\beta - 1)} \right]^{1/4} \\ \sim 3 \times 10^3 L_{53}^{1/4} t_{v,-3}^{-1/4} \varepsilon_{\text{peak,MeV}}^{-1/4}, \quad (70)$$

in the VHLF range, because the photon density is almost constant below $\varepsilon_{\text{peak}}$ for the usual spectral index. We note that the exponential cutoff is usually smoothed to a broken power-law by multizone effects (Aoi et al. 2009; Li 2010a; Granot et al. 2008; Bosnjak et al. 2009).

(2) The second possibility is the cooling break at

$$\nu_c = 9 \text{ GeV } \Gamma_4^8 L_{53}^{-3/2} t_{v,-3} \varepsilon_{B,-2}^{-3/2}, \quad (71)$$

in Eq. (60). Thus, the break at ~ 1.4 GeV suggests a VHLF of $\Gamma \sim 10^4$. The change in the spectral index at the cooling break is 0.5 in Eq. (61), which can be used as a test of this possibility, although the photon number is insufficient in the current observations. If the low-energy part below the cooling break is produced by the spectral integration in Eq. (64), the change of the index is smaller than 0.5.

(3) The third possibility is the maximum synchrotron cutoff,

$$\nu_{\text{max}}^{\text{cool}} = \phi_s \frac{3q_e B'}{4\pi m_e c} \gamma'_{\text{max}}{}^2 \Gamma = \phi_s \frac{27}{16\pi} \frac{m_e c^3}{e^2} \frac{\Gamma}{\kappa} = 50 \kappa^{-1} \Gamma_3 \text{ GeV}, \quad (72)$$

which is only dependent on the bulk Lorentz factor Γ , and is determined by the balance between the acceleration time $t'_{\text{acc}} = \kappa \gamma'_e m_e c / q_e B'$ and the cooling time $t'_{\text{cool}} = 3m_e c / 4\sigma_T U'_B \gamma'_e$, so $\gamma'_{\text{max}} = (6\pi q_e / \kappa \sigma_T B')^{1/2}$, where the coefficient $\phi_s = 0.2294$ is quoted from Wijers and Galama (1999) (Wijers & Galama 1999). If the break at ~ 1.4 GeV is due to the maximum synchrotron cutoff limited by the cooling time $\nu_{\text{max}}^{\text{cool}}$, the shock acceleration has to be much slower than the Bohm limit, $\kappa \sim 50 \Gamma_3 \gg 1$, i.e., the scattering mean free path is much larger than the Larmor radius. Apart from the break in GRB 090926, the VHLF models ($\Gamma \sim 10^4$) predict the maximum synchrotron cutoff in the TeV region for $\kappa \sim 1$, which is a nice target for the future Cherenkov Telescope Array (CTA) Project (see Fig. 5).

On the other hand, if $\nu_{\text{max}}^{\text{cool}} < \nu_c$, i.e., $\Gamma \gtrsim 10^4$, the maximum synchrotron cutoff is limited by the dynamical time $t'_{\text{dyn}} = \Gamma t_v > t'_{\text{acc}}$, rather than by the cooling time, yielding $\gamma'_{\text{max}} = q_e B' \Gamma t_v / \kappa m_e c$, and hence,

$$\nu_{\text{max}}^{\text{dyn}} = 0.1 \text{ GeV } \Gamma_5^{-6} L_{53}^{3/2} \varepsilon_{B,-2}^{-3/2} t_{v,-3}^{-3} \kappa^{-2}. \quad (73)$$

Therefore, the break at ~ 1.4 GeV could be produced by VHLF flows with $\Gamma \sim 6 \times 10^4$. It is a unique feature for the

VHLF models to be able to accompany the maximum synchrotron cutoff limited by the dynamical time, not by the cooling time.

(4) The last possibility is that the extra component of GRB 090926 might be the e^\pm annihilation line from the photosphere at the blueshifted energy,

$$\nu_\pm = \Gamma m_e c^2 \sim 0.5 \text{ GeV } \Gamma_3, \quad (74)$$

which is broadened by the order-of-unity distribution of the Lorentz factor on the photosphere (Ioka et al. 2007; Murase & Ioka 2008). This scenario might be possible if the e^\pm pairs are continuously created on the photosphere, although the mechanism for the e^\pm creation is not apparent.

4.4. GeV onset delay

Fermi discovered that the high-energy emission (> 100 MeV) is delayed behind the onset of the MeV emission in almost all LAT GRBs. The delay time in the rest frame is $t_{\text{delay}} \sim 1$ s for long GRBs and ~ 0.1 s for short bursts, GRB 081024B and GRB 090510. These delays are not just caused by the flux increases above the LAT detection threshold, but by the spectral changes in the Band and/or extra components at least in the well-observed bursts. Since the observed delays of the extra component are larger than the variability timescale of the Band component, ~ 0.01 – 0.1 s, the physical origin of the delay is not likely the kinematic effect (Toma et al. 2010).

In the hot photosphere–internal–external shock model in §4.1 and Fig. 4, the GeV delayed phase arises when the emission from internal and external shocks is weaker than the photospheric emission, i.e., almost all the energy escapes in the form of the photospheric luminosity, not the kinetic luminosity. This is realized for the dimensionless entropy in the moderate range $\eta_* \sim 10^3 < \eta < \eta_{k1} \sim 10^4$ according to the dissipative hot photosphere model in Table 1, Fig. 3, and Eqs. (23) and (36). On the other hand, in the GeV bright phase, the kinetic luminosity is comparable to the photospheric luminosity, i.e., in the high-entropy range $\eta_{k1} \sim 10^4 < \eta < \eta_{k3} \sim 10^7$ in Table 1, Fig. 3, and Eqs. (36) and (38), which is also the VHLF range.

Therefore, in our picture, the baryon loads decrease progressively from the GeV delayed phase to the GeV bright phase, across the critical entropy $\eta \sim \eta_{k1}$ in Eq. (36) and Fig. 3. As argued in §§3.1 and 3.2, the baryon is entrained at the dissipation radius r_m , which is a function of η in Eq. (35). Then, we can predict the delay time as the light crossing time of the dissipation radius for $\eta = \eta_{k1}$,

$$t_{\text{delay}} \sim \frac{r_m(\eta_{k1})}{c} \sim \frac{r_b}{c} \sqrt{\Gamma_s \eta_{k1}} \sim 0.5 \text{ s } L_{53}^{3/5} T_{600\text{keV}}^{-8/5} \Gamma_s^{1/5}, \quad (75)$$

where r_b is the base size of the flow in Eq. (9). Interestingly, this predicted timescale is comparable to the observed delay time $t_{\text{delay}} \sim 0.1$ – 1 s. This coincidence also supports our picture that the VHLF fireballs are responsible for the extra high-energy emission. In addition, Eq. (75) combined with the $\varepsilon_{\text{peak}}$ – L Yonetoku relation in Eq. (1) gives

$$t_{\text{delay}} \sim \frac{r_m(\eta_{k1})}{c} \sim \frac{r_{pp}(\eta_{k1})}{c} \sim 0.5 \text{ s } L_{53}^{-1/5} \Gamma_s^{1/5}, \quad (76)$$

which has a weak dependence on the luminosity, consistent with the observations. Further observations of the delay time would discriminate models since other models have different parameter dependences. For example, if the Coulomb

collisions control the kinetic luminosity, the delay time is $t_{\text{delay}} \sim r_m(\eta_C) \propto L^{-1/6} \Gamma_s^{1/9} f_{\pm}^{1/9}$ with the critical entropy η_C in Eq. (51). The delay caused by the e^{\pm} creation cutoff also has a different dependence $t_{\text{delay}} \propto L\Gamma^{-6}$ (Li 2010a). If we can refine the delay time measurements in the future, the delay time might be used as a distance indicator like the $\varepsilon_{\text{peak}}-L$ Yonetoku relation.

The delay timescale is also comparable to the light crossing time of the progenitor star

$$t_{\text{delay}} \sim \frac{R_{\text{star}}}{c} \sim 0.3 \text{ s} \left(\frac{R_{\text{star}}}{10^{10} \text{ cm}} \right). \quad (77)$$

Therefore, a natural picture is that the fireball dissipation via baryon loads is controlled by the environment just outside the star. As the environment changes with time $\sim R_{\text{star}}/c$, the baryon loads decrease and the dissipation radius increases beyond the thermalization radius, leading to a VHLF fireball via the collisionless bulk acceleration in §3.4, and hence, to the high-energy emission with the onset delay.

Although we have used the light crossing time to estimate the timescales, the actual environment could be more complex, which may not be governed by the light speed. After the jet breakout, the jet is likely surrounded by a cocoon, which consists of the decelerated jet and the shocked stellar envelope. The velocity of the cocoon depends on the jet luminosity and the stellar structure, although it is typically $v_c/c \sim 0.1-1$ (Toma et al. 2007). If the accelerated particles are important for the baryon loading, the typical velocity is the light speed. The baryon loading process is not clear, and further discussions are given in §§5.3, 5.4, and 5.5.

5. PREDICTIONS AND OPEN ISSUES

5.1. TeV neutrino

We can predict \sim TeV neutrinos and their temporal anticorrelation with extra GeV high-energy γ -rays in the hot photosphere–internal–external shock model in §4.1 and Fig. 4. In this model, the baryon (protons) is loaded below the photosphere, leading to the fireball dissipation as suggested by observations (see §3.1). The entrained protons are relativistic in the comoving frame of the shocked fireball with the Lorentz factor $\gamma'_p \sim \Gamma_m/2\Gamma_s \sim \sqrt{\eta/\Gamma_s}/2$ in Eqs. (20) and (35). The pp collisions between these protons produce pions, which immediately decay into neutrinos (Paczynski & Xu 1994; Derishev et al. 1999; Bahcall & Mészáros 2000; Mészáros & Rees 2000b) via

$$\pi^+ \rightarrow \mu^+ + \nu_\mu \rightarrow e^+ + \nu_e + \bar{\nu}_\mu + \nu_\mu, \quad (78)$$

$$\pi^- \rightarrow \mu^- + \bar{\nu}_\mu \rightarrow e^- + \bar{\nu}_e + \nu_\mu + \bar{\nu}_\mu. \quad (79)$$

Each neutrino shares $\sim m_\pi/4m_p \sim 5\%$ of the primary proton energy, so that the observed neutrino energy is

$$\varepsilon_\nu \sim \frac{m_\pi}{4m_p} \Gamma_m \gamma'_p m_p c^2 \sim 0.2 \text{ TeV} \left(\frac{\eta}{10^4} \right). \quad (80)$$

The neutrino luminosity originates from the proton kinetic luminosity, which also produces the extra GeV γ -ray component in our model. That is, the same kinetic energy is shared by neutrinos and extra γ -rays. Therefore, the \sim TeV neutrinos are predicted to anticorrelate with GeV γ -rays, as shown in Fig. 6 and Table 1. Such a temporal prediction would be interesting for the upcoming multimessenger astronomy. The neutrino fluence may be comparable to the MeV γ -ray fluence

since the kinetic energy is comparable to the photospheric energy, as shown in Eq. (18) and Table 1. However, as discussed in §4.4, the pp collision is effective only in the GeV delay phase with a timescale $\sim t_{\text{delay}} \sim 1$ s less than the total duration $T \sim 20$ s. Therefore, the neutrino fluence would be $\sim t_{\text{delay}}/T \sim 0.05$ times less than the MeV γ -ray fluence $\mathcal{F} \sim 10^{-6} \text{ erg cm}^{-2}$. With the GRB event rate $R_{\text{GRB}} \sim 10^3 \text{ yr}^{-1}$, the diffuse neutrino background from GRBs is estimated as

$$\varepsilon_\nu^2 \Phi_\nu \sim \frac{1}{4\pi} \frac{t_{\text{delay}}}{T} \mathcal{F} R_{\text{GRB}} \sim 1 \times 10^{-10} \text{ GeV cm}^{-2} \text{ s}^{-1} \text{ sr}^{-1} \quad (81)$$

which is less than the current limits (Abbasi et al. 2010, 2009; Fukuda et al. 1992) and less than the IceCube design sensitivity by an order of unity. If the GeV bright bursts are a minor population as the LAT bursts are $\sim 7\%$ of Fermi bursts, the diffuse neutrino flux is higher by $\sim T/t_{\text{delay}} \sim 20$, i.e., comparable to the diffuse γ -ray flux from GRBs, which could be detectable using IceCube in the near future. We note that IceCube is sensitive to neutrinos above TeV energy, and not so much to sub-TeV neutrinos in Eq. (80). However, a fraction of protons would have the random Lorentz factor larger than γ'_p in Eq. (80), as discussed in §3.2, so that the detection is not completely hopeless.

The photomeson interactions ($p\gamma \rightarrow n\pi$) could also generate pions, and hence, neutrinos if the photon spectrum under the photosphere is already nonthermal, as discussed in §3.5. Each neutrino energy is also similar to the pp collisional case in Eq. (80), since the primary proton energies are the same. We also expect the anticorrelation between \sim TeV neutrinos and GeV γ -rays in Fig. 6 as in the pp collisional case because the energy source is again the proton kinetic energy, which also produces the extra GeV γ -ray component. However, the neutrino luminosity is suppressed by the factor in Eq. (49) compared with the proton kinetic luminosity because the Bethe-Heitler process also occurs simultaneously and consumes the proton energy into e^{\pm} creation. Therefore, the photomeson neutrinos may be difficult to detect unless the photon index is hard $\beta < 2$ in Eq. (49).

The neutrino emission could precede the γ -ray emission when the jet is still inside the progenitor star (Razzaque et al. 2003; Pruet 2003). In this case, the accelerated protons interact with matter of the progenitor star or synchrotron photons. The γ -rays cannot escape owing to the large optical depth. The time delay between neutrinos and γ -rays is expected to be about $R_{\text{star}}/v_j \sim 1-10$ s, approximately the time taken by the jet to emerge from the progenitor star (Toma et al. 2007).

Wang and Dai (Wang & Dai 2009) and Murase (Murase 2008) also discussed the high-energy neutrino emission from the dissipative photospheres of GRBs. We can predict that the high-energy neutrinos in their models would also temporally anticorrelate with the GeV γ -rays.

5.2. MeV γ -ray spectrum

In the photosphere model, it is unclear how to produce the high-energy nonthermal tail of the Band spectrum (Ioka et al. 2007). The main problem is the source of the nonthermal energy that is comparable to the total energy. The nonthermal tail has to be produced near the photosphere $\tau_T \sim 1$, since the spectrum is thermalized above the observed frequency,

$$\nu_{\text{th}} \sim \frac{\Gamma m_e c^2}{\tau_T} \sim 500 \text{ MeV} \left(\frac{\Gamma}{10^4} \right) \left(\frac{\tau_T}{10} \right)^{-1}, \quad (82)$$

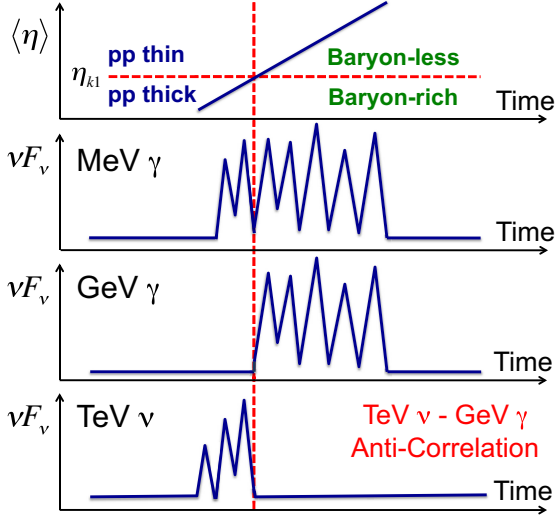


FIG. 6.— The anticorrelation between \sim TeV neutrinos and extra variable GeV γ -rays is schematically shown. This is predicted independently of the neutrino generation processes, either pp or photomeson interactions, because the same proton kinetic energy is shared by neutrinos and extra GeV γ -rays in the hot photosphere–internal–external shock model in §4.1 and Fig. 4. In our picture of §4.4, the GeV onset delay phase corresponds to the baryon-rich (low entropy) phase, associated with the effective pp neutrino emission with \sim TeV energy in Eq. (80) and the diffuse flux in Eq. (81).

through Compton scatterings by the thermal electrons with temperature T'_e less than that of the nonthermal photons. This is because a photon changes its energy by $\Delta\nu'_\gamma/\nu'_\gamma \sim (4kT'_e - \nu'_\gamma)/m_e c^2$ in a single scattering, so that a relatively large optical depth $\tau_T \sim \nu'_\gamma/\Delta\nu'_\gamma \sim m_e c^2/\nu'_\gamma$ is necessary for thermalization at $\nu'_\gamma > 4kT'_e$. Note that the necessary optical depth is not $\tau_T \sim (\nu'_\gamma/\Delta\nu'_\gamma)^{1/2}$ here, since the fireball is expanding with decreasing τ_T .

As a by-product of the discussions in the previous sections, we could find a hint for the energy source of the high-energy nonthermal Band spectrum in the photosphere model. That is the relativistic baryon (protons) component loaded below the photosphere at the fireball dissipation, as suggested by observations (see §3.1). The entrained protons are relativistic in the comoving frame of the shocked fireball (see §3.2), and hence, can heat electrons via pp collisions (see §3.3), $p\gamma$ (Bethe-Heitler and photomeson) processes, and Coulomb collisions with e^\pm created by pp and $p\gamma$ processes (see §3.5). Then, the heated e^\pm can produce the nonthermal broken power-law spectrum through the unsaturated Comptonization of the thermal photons. The total proton energy before thermalization is just comparable to the photospheric radiation energy in Eq. (18), as required by the nonthermal tail of the Band spectrum. This energy equipartition comes from the energy and momentum conservation in Eqs. (11) and (12) without fine tuning. For the electron heating near the photosphere $\tau_T \sim 1$, the VHLF range $\eta > \eta_{k1}$ may be preferred because the dissipation radius r_m is near or above the baryonic photosphere r_{ph} (see Fig. 3).

Alternatively, the plasma turbulence could be initiated at the baryon loading, at least with mildly relativistic velocities. Since each fluid element has a relative velocity, the turbulence would scatter thermal photons to a broken power-law spectrum, where the Y -parameter can be of order unity for the dissipation near the photosphere. The turbulence will be damped within the eddy turnover time. However, once a nonthermal

spectrum is formed, the spectral shape is almost preserved below ν_{th} in Eq. (82).

Beloborodov (2009) (Beloborodov 2009) (see also Ref. Derishev et al. (1999)) has recently shown that the pn , pp , and Coulomb collisions can heat e^\pm to produce the nonthermal Band spectrum in the context of the neutron-loaded fireballs. Since the neutron models only produce mildly relativistic nucleons, it is interesting to calculate the case of the relativistic protons and neutrons in the shocked fireball frame. In contrast to the neutron models, the $p\gamma$ (Bethe-Heitler and photomeson) processes are also important for the relativistic case as shown in §3.5. The $p\gamma$ processes have an advantage that the random Lorentz factor of protons does not drop to unity in most cases (see §3.5), and hence, the fireball can realize both the nonthermal photospheric spectrum and the fair fraction of kinetic energy for the internal and external shocks at the same time, in contrast to the pp collisions. Kazanas et al. (Kazanas et al. 2002; Mastichiadis & Kazanas 2009) also considered the relativistic proton accumulation and the Bethe-Heitler process in the supercritical pile model, which may be relevant to the late evolution above the photosphere.

5.3. Origin of the $\varepsilon_{\text{peak}}-L$ Yonetoku relation

Thus far, we have just used the $\varepsilon_{\text{peak}}-L$ Yonetoku relation in Eq. (1) as an empirical relation. Let us consider the physical origin of this relation in the dissipative hot photosphere model. As discussed in §3.1, the $\varepsilon_{\text{peak}}-L$ Yonetoku relation is reproduced by the fireball dissipation under the photosphere that is associated with the deceleration of the fireball, probably via the baryon loading. The necessary (isotropic) baryon loading rate \dot{M} can be obtained from Eqs. (9), (19), and (35), without using the Yonetoku relation, as

$$\dot{M} \sim \frac{L\Gamma_s r_b^2}{c^2 r_m^2} \sim 10^{-5} M_\odot \text{ s}^{-1} \Gamma_s r_{m,10}^{-2} L_{53}^2 T_{600\text{keV}}^{-4}. \quad (83)$$

Interestingly, the dependence $L^2 T^{-4}$ disappears if the $\varepsilon_{\text{peak}}-L$ Yonetoku relation in Eq. (1) is satisfied. The remaining dependence in Eq. (83) is the Lorentz factor of the slow mass Γ_s and the baryon loading radius (dissipation radius) r_m , which are all determined by the environment that supplies the baryon into the jet. In other words, the $\varepsilon_{\text{peak}}-L$ Yonetoku relation is satisfied if the baryon loads are controlled by the environment and do not differ event by event so much. This picture is also consistent with the fact that the GeV onset delay is controlled by the environment in §4.4. However, it is still difficult to derive the normalization of the baryon loading rate, partly because the current MHD numerical simulations have not yet implemented the key physical processes of radiation transfer and e^\pm creation (Lazzati et al. 2009; Zhang et al. 2004; Mizuta et al. 2004, 2010). For Eq. (83), the essential relation is $\Gamma_m \propto \sqrt{\eta}$ in Eqs. (17) and (35), which states that the fireballs are relativistic even after the dissipation, derived from the new Equations (11) and (12).

5.4. Baryon load and jet structure

As discussed in §3.1, the $\varepsilon_{\text{peak}}-L$ Yonetoku relation in Eq. (1) suggests the fireball dissipation under the photosphere that accompanies the deceleration of the fireball, probably via the baryon loading. However, the actual baryon loading process is unclear, partly because the current MHD numerical simulations have not yet implemented the key physical

processes of radiation transfer and e^\pm creation (Lazzati et al. 2009; Zhang et al. 2004; Mizuta et al. 2004, 2010).

From the kinematical viewpoints, we may argue that the baryon loading process would require the nonspherical configuration. Otherwise, the radiation-dominated outflow from the central engine with the initial width $r_0 \sim 10^7$ cm cannot be fully dissipated at the dissipation radius r_m in most cases. We can show this by comparing r_m with the radius where the rapid outflow with width $r_0 \sim 10^7$ cm completely runs into the shocked region with the Lorentz factor Γ_m as

$$\frac{r_0 \Gamma_m^2}{r_m} \sim \frac{\Gamma_m}{r_b/r_0} \sim \frac{\sqrt{\Gamma_s \eta}}{10 L_{53}^{1/2} T_{600\text{keV}}^{-2}}, \quad (84)$$

with Eqs. (9) and (35). This ratio is larger than unity, i.e., the dissipation is not completed at r_m , for almost all parameter regions $\eta \gtrsim 10^2 \Gamma_s^{-1}$ in Fig. 3. This problem of the incomplete dissipation applies to all dissipative photosphere models with $\Gamma \gtrsim 10^2$ and $L_{\text{ph}} \sim L$. In other words, the one-dimensional picture of the spherical reverse and forward shocks is insufficient to explain the GRB observations in the photosphere model. The picture should be rather close to the complete merger with turbulence.

The nonspherical configuration may be plausible because the low-entropy fireball is pushed by the high-entropy fireball and the system is subject to the Rayleigh-Taylor instability and/or the plasma instabilities (Waxman & Piran 1994; Ioka et al. 2007). Then, the full dissipation condition ($r_m > \Gamma_m^2 r_0$ in the above) would be replaced by $r_m > \Gamma_s^2 r_0$ that is easily satisfied. One may also consider a jet configuration of the fireball that entrains baryon (protons and neutrons (Levinson & Eichler 2003)) through the boundary of the jet. If the central engine works intermittently, the baryon surrounding the jet, previously in pressure equilibrium with the jet, will enter the funnel sideways. As long as the jet opening angle $\theta_j (> \Gamma_r^{-1})$ is smaller than the causal angle Γ_m^{-1} , the fireball can be fully dissipated via turbulence, e.g., caused by the Kelvin-Helmholtz instability (Goodman & MacFadyen 2008; Sironi & Goodman 2007; Zhang et al. 2009). Note that the jet opening angle remains constant after the jet reacceleration because the causal angle shrinks all the time.

Although the causal angle $\Gamma_m^{-1} \sim 0.01 \eta_4^{-1/2} \Gamma_s^{-1/2}$ for the high entropy flow with $\eta > 10^4$ may be smaller than the conventional opening angle $\theta_j \sim 0.1$, the jet could have two components or a continuous structure with the high entropy flow surrounded by the low to moderate entropy flow of $\eta \sim 10^2 - 10^4$. We note that the two-component jet is suggested for GRB 080319B (Racusin et al. 2008). If this is the case, the extra GeV component associated with the high entropy flow (see Table 1) may be observed only from the viewing angle near the jet center, possibly consistent with the fact that not all observed bursts are bright with GeV γ -rays.

The initial variability time $\sim r_0/c \sim 3 \times 10^{-4}$ s reflecting the central engine size could be preserved at the dissipation since the successive shells may not contact with each other for $r_m < r_0 \Gamma_m^2$ in Eq. (84). If the dissipation is nonspherical as discussed above, the timescale could instead be determined by the crossing time of the causal region, $r_m/c \Gamma_m = r_b/c \sim 3 \times 10^{-3}$ s, with Eqs. (9) and (35).

5.5. Multiple baryon loads

The baryon-loaded shell could expand and collide before coasting against another slow mass M_{s2} with a Lorentz factor

Γ_{s2} . This second merger is characterized by the dimensionless entropy $\eta_2 = E_r/\Gamma_r/M_{s2}c^2$, since the rapid shell is radiation-dominated as in the first merger. The merger is divided into three types:

- (1) If $\eta_2 > \Gamma_r^2/\Gamma_{s2}$, we may neglect the second merger since the rapid shell is not sufficiently decelerated and the fireball temperature is almost constant.
- (2) If $\eta_2 < \eta$, the total amount of baryon is determined by the second merger. The Lorentz factor of the fireball goes down to $\Gamma_{m2} \sim \sqrt{\Gamma_{s2}\eta_2}$ and then up to $\Gamma_{c2} \sim \eta_2$ with a different base radius $r_{b2} \sim r_{m2}/\Gamma_{m2}$. We may consider that the initial condition of the dissipated fireball is reset by the second merger.
- (3) If $\eta < \eta_2 < \Gamma_r^2/\Gamma_{s2}$, the total amount of baryon is not changed so much, while the fireball is decelerated to have a different temperature and base radius. The initial radius of the dissipated fireball is not $r_m/r_b \sim \Gamma_m \sim \sqrt{\Gamma_s \eta}$, but $r_{m2}/r_b \sim \Gamma_{m2} \sim \sqrt{\Gamma_{s2}\eta_2}$ that tends to bring the dotted line upward in Fig. 3. As a result, we have different critical entropies from $\eta_{k1}, \eta_{k2}, \eta_{k3}$ in Eqs. (36), (37), (38), and therefore, a different maximum Lorentz factor from $\Gamma_{c,\text{max}}, \Gamma_{c,\text{max}}^c$ in Eqs. (41), (42). It is straightforward to obtain these quantities in this case.

We note that the last value of the base radius determines the observed relation in Eq. (9).

If the merger type is (3), the necessary baryon loading rate becomes different from that in Eq. (83). Therefore, the merger type (3) could introduce an outlier in the Yonetoku relation, if the origin of the Yonetoku relation is correct in §5.3. To have a tight Yonetoku relation, the baryon loading needs to be larger at the outermost radius, which may be reasonable since the jet boundary also becomes larger.

5.6. Early X-ray afterglow

Swift discovered the steep and shallow decay phase in the early X-ray afterglows (Zhang et al. 2006; Ioka et al. 2006; Panaitescu et al. 2006; Zhang et al. 2006; Huang et al. 2006; Sato et al. 2007). The important point of these observations is that the early X-ray afterglows are too dim for the conventional internal-external shock model, in which the kinetic energy left for the afterglow emission is comparable to or usually larger than the prompt energy released at the internal shocks, so-called the internal shock efficiency problem (Ioka et al. 2006). In the hot photosphere-internal-external shock model in Fig. 4 and Table 1, this is not a problem because the kinetic energy fraction of the afterglow may be relatively small for the moderate entropy range $\eta_*(\sim 10^3) < \eta < \eta_{k1}(\sim 10^4)$ in Table 1, where the fireball becomes optically thin in the accelerating phase before converting all the radiation energy into kinetic energy.

On the other hand, the LAT bursts with bright GeV γ -rays do not seem to be associated with the steep and shallow X-ray afterglows, although more events are necessary to confirm this fact. In these bursts, the kinetic energy fraction of the afterglow may be larger than that of the *Swift* bursts. This may be consistent with our picture that the extra GeV emission is produced by the relatively high entropy fireball with $\eta > \eta_{k1}(\sim 10^4)$ in the VHLF range, whose kinetic luminosity is comparable to the photospheric luminosity, as shown in

Table 1. If the jet is structured with the high entropy flow surrounded by the moderate entropy flow as discussed in §5.4, the shallow decay in *Swift* events may be detected for observers in the direction of the moderate entropy flow, since the high-entropy region with large kinetic energy is progressively seen as the afterglow is decelerated (Toma et al. 2006).

5.7. Short GRB: magnetized jet from white dwarf?

Short LAT GRBs 081024B and 090510 have smaller GeV delay time, $t_{\text{delay}} \sim 0.1$ s, than long GRBs. According to §4.4, this implies that the size of the progenitor for short GRBs is smaller than that for long GRBs. Interestingly, the inferred size $ct_{\text{delay}} \sim 10^9$ cm is comparable to the white dwarf radius. The white dwarf model may also be favorable to explain the extended emission observed in the short GRBs, since the accretion time of the white dwarf material into the central engine can be much longer than the neutron star case, where the neutron star accretion is too fast to explain the long timescale (> 100 s) of the extended emission (Barthelmy et al. 2005; Norris & Bonnell 2006).

For short GRBs, the LAT (\sim GeV) fluence is comparable to and even larger than the GBM (\sim MeV) fluence, in contrast to long GRBs with the LAT-to-GBM fluence ratio of ~ 0.1 (Ghisellini et al. 2010). This may require a modification to the simple version of our model, because the extra GeV luminosity is usually less than the photospheric luminosity in Eq. (62). One possibility is that the short GRBs could have a low entropy phase with $\eta < \eta_*$ (baryon-rich phase), in which the photospheric emission is suppressed below the kinetic one (see Table 1). The other possibility is a magnetized fireball jet because magnetic fields are not radiated away at the photosphere, reducing the photospheric emission (see §3.7). The magnetic fields also increase the kinetic energy by pushing the matter even above the photosphere via the magnetic pressure, which could enhance the GeV emission.

6. SUMMARY

We have investigated the fireball model with dissipation under the photosphere, as suggested by the observed spectral $\varepsilon_{\text{peak}}-L$ Yonetoku relation in Eq. (1) (§3.1). We find that the fireball can entrain the relativistic baryon component at the dissipation, with energy comparable to the radiation component, as derived from the energy and momentum conservation in Eqs. (11) and (12). The relativistic baryon (proton) component can alter the GRB fireball dynamics and spectra in novel ways, which we have studied in this paper. Our main results may be summarized as follows.

- As outlined in §2, the relativistic baryon component can reexpand to a very high Lorentz factor (VHLF) $\Gamma \sim 10^3-10^6$, much larger than the conventional upper limit $\Gamma \lesssim 10^3$, (§3.4, Figs. 1 and 3). Since the pressure is provided by the relativistic collisionless motions of protons (and the magnetic field generated by these protons), this mechanism may be called the collisionless bulk acceleration. The VHLF is achieved when the baryon load is low (i.e., high entropy) without efficient thermalization of protons via pp , $p\gamma$ (Bethe-Heitler and photomeson), Coulomb, and plasma interactions (§§3.3 and 3.5). The kinetic energy can become comparable to the total energy in the VHLF fireballs (§3.2, Table 1, Fig. 3), which can alter the internal and external shock emission (see below). These VHLF models are currently consistent with previous observations (§3.6).

- The VHLF fireballs can explain the extra variable GeV component in the GRB spectrum using the simple internal shock synchrotron emission. In the VHLF models, a single emission mechanism (synchrotron emission) can make a rising power-law spectrum over >7 energy digits, and the internal shock efficiency can also be sufficiently high to produce the emission energy comparable to the total one, as observed by Fermi/LAT. The VHLF emission is also a nice target for the future Cherenkov Telescope Array (CTA), since the e^\pm creation cutoff goes beyond the TeV range in the VHLF models. The main Band component may be attributed to the photospheric emission, and the long-lived GeV component to the external shock in this hot photosphere–internal–external shock synchrotron model (§§4.1 and 4.2, Fig. 4).
- In the VHLF models, the spectral break at ~ 1.4 GeV observed in the extra component of GRB 090926 is not caused by the e^\pm creation cutoff with $\Gamma \sim 600$ (§4.3). The spectral break could be the synchrotron cooling break for $\Gamma \sim 10^4$, or the maximum synchrotron cutoff, particularly limited by the dynamical time (not by the cooling time) for $\Gamma \sim 10^5$.
- The observed GeV onset delay can be naturally explained in the dissipative hot photosphere model because the baryon loads at the dissipation would be rich shortly after the jet breakout, and hence, the relativistic baryon component is thermalized into radiation in the fireball, leaving little kinetic energy for the GeV emission (§4.4). The timescale of the GeV onset delay can be calculated from the theory as the timescale at the dissipation radius, i.e., the timescale to change the baryon loading rate, and hence, the environment around the progenitor star. The predicted delay time ~ 0.5 s and also its weak dependence on the luminosity $t_{\text{delay}} \propto L^{-1/5} \sim L^{-1/6}$ in Eq. (76) are consistent with the observations.
- The dissipative hot photosphere model predicts \sim TeV neutrinos in Eq. (80) and the anticorrelation between \sim TeV neutrinos and the extra variable GeV γ -rays, independently of the neutrino generation processes, either pp or photomeson interactions, because the same proton kinetic energy is shared by neutrinos and extra GeV γ -rays. In the optimistic case, the diffuse neutrino background from GRBs in Eq. (81) could be detected using IceCube in the near future.
- The relativistic baryon component loaded into the fireball at the dissipation could work as the as-yet-unknown energy source to deform the photospheric thermal spectrum into the nonthermal Band spectrum (§5.2). Without fine tuning, the relativistic baryon component has the right amount of energy (comparable to the thermal energy) to make the nonthermal tail (§3.2). The protons could heat e^\pm via pp , $p\gamma$ (Bethe-Heitler and photomeson), and Coulomb interactions, leading to the Comptonization of the thermal photons into the broken power-law spectrum. Alternatively, the mildly relativistic plasma turbulence induced by the baryon loading could make the nonthermal spectrum. Further investigations in this direction appear interesting.

- The spectral $\varepsilon_{\text{peak}}-L$ Yonetoku relation can be reproduced by the fireball dissipation if the baryon loading rate is determined by the environment that is nearly identical to any bursts in Eq. (83). Nearly identical environments could be plausible if GRBs are produced by a certain class of progenitor. For the derivation of the $\varepsilon_{\text{peak}}-L$ Yonetoku relation, it is important that the fireballs are relativistic even after the dissipation, as deduced from the energy and momentum conservation in Eqs. (11) and (12).
- The actual baryon loading process at the dissipation has not been clarified. From the kinematics, the dissipation process would require the nonspherical configuration, such as the turbulence and/or the jet boundary (§5.4). In the jet case, the causality argument suggests a two-component or structured jet.
- A structured jet with both the radiation-dominated and VHLF flows could explain the steep/shallow decay of

early X-ray afterglows observed in the *Swift* bursts (as viewed from the radiation-dominated flow) and the possible paucity of the steep/shallow decay phase in the Fermi/LAT bursts (as viewed from the VHLF flow) in a unified fashion (§5.6).

- We have speculated that the short GRBs might accompany the magnetized or baryon-rich jet (for the high GeV fluence ratio) from the white dwarf progenitor (for the short GeV onset delay) (§5.7).

We thank K. Asano, N. Kawanaka, D. Kazanas, P. Mészáros, A. Mizuta, K. Murase, T. Nakamura, Y. Ohira, F. Takahara, M. Teshima, K. Toma, X. Y. Wang, and R. Yamazaki for useful discussions. This work is supported in part by Grants-in-Aid from the Ministry of Education, Culture, Sports, Science and Technology (MEXT) of Japan, Nos.19047004, 21684014, and 22244019.

REFERENCES

- A. A. Abdo et al. (Fermi GRB/LAT Collaborations), *ApJ*, 706 (2009a) L138.
A. A. Abdo et al., *Science*, 323 (2009b) 1688.
A. A. Abdo et al. (Fermi GRB/LAT Collaborations), *Nature*, 462 (2009c) 331.
A. A. Abdo et al. (Fermi GBM/LAT Collaborations), *ApJ*, 707 (2009d) 580.
A. A. Abdo et al. (Fermi GRB/LAT Collaborations), *ApJ*, 712 (2010a) 558.
A. A. Abdo et al. (Fermi GRB/LAT Collaborations), *ApJ*, 712 (2010b) 558.
A. A. Abdo et al. (Fermi GRB/LAT Collaborations), arXiv:1005.2141 (2010c).
R. Abbasi et al. (IceCube Collaboration), *ApJ*, 701 (2009) 1721 [Errata: 708 (2010) 911].
R. Abbasi et al. (IceCube Collaboration), *ApJ*, 710 (2010) 346.
L. Amati, arXiv:1002.2232 (2010).
L. Amati, F. Frontera and C. Guidorzi, *Astron. Astrophys.*, 508 (2009) 173.
J. Aoi, K. Murase, K. Takahashi, K. Ioka and S. Nagataki, arXiv:0904.4878 (2009).
K. Asano and T. Terasawa, *ApJ*, 705 (2009) 1714.
K. Asano, S. Inoue and P. Meszaros, *ApJ*, 699 (2009a) 953.
K. Asano, S. Guiriec and P. Mészáros, *ApJ*, 705 (2009b) L191.
J. N. Bahcall and P. Mészáros, *PRL*, 85 (2000) 1362.
M. G. Baring and A. K. Harding, *ApJ*, 491 (1997) 663.
R. Barniol Duran and P. Kumar, arXiv:1003.5916 (2010).
S. D. Barthelmy et al., *Nature*, 438 (2005) 994.
A. M. Beloborodov, *ApJ*, 539 (2000) L25.
A. M. Beloborodov, arXiv:0907.0732 (2009).
Z. Bosnjak, F. Daigne and G. Dubus, *Astron. Astrophys.*, 498 (2009) 677.
G. Cavallo and M. J. Rees, *Mon. Not. R. Astron. Soc.*, 183 (1978) 359.
M. J. Chodorowski, A. A. Zdziarski and M. Sikora, *ApJ*, 400 (1992) 181.
A. Corsi, D. Guetta and L. Piro, arXiv:0905.1513 (2009a).
A. Corsi, D. Guetta and L. Piro, arXiv:0911.4453 (2009b).
M. De Pasquale et al., *ApJ*, 709 (2010) L146.
E. V. Derishev, V. V. Kocharovsky and V. V. Kocharovsky, *ApJ*, 521 (1999) 640.
E. V. Derishev, V. V. Kocharovsky and V. V. Kocharovsky, *Astron. Astrophys.*, 372 (2001) 1071.
Y. Z. Fan, *Mon. Not. R. Astron. Soc.*, 397 (2009) 1539.
Y. Z. Fan, *Mon. Not. R. Astron. Soc.*, 403 (2010) 483.
Y. Z. Fan, T. Piran, R. Narayan and D. M. Wei, *Mon. Not. R. Astron. Soc.*, 384 (2008) 1483.
S. Fukuda et al. [Super-Kamiokande], *ApJ*, 578 (1992) 317.
G. M. Fuller, J. Pruet and K. Abazajian, *PRL*, 85 (2000) 2673.
W. H. Gao, J. R. Mao, D. Xu and Y. Z. Fan, *ApJ*, 706 (2009) L33.
G. Ghisellini and A. Celotti, *ApJ*, 511 (1999) L93.
G. Ghisellini, A. Celotti and D. Lazzati, *Mon. Not. R. Astron. Soc.*, 313 (2000a) L1.
G. Ghisellini, D. Lazzati, A. Celotti and M. J. Rees, *Mon. Not. R. Astron. Soc.*, 316 (2000b) L45.
G. Ghisellini, A. Celotti, G. Ghirlanda, C. Firmani and L. Nava, *Mon. Not. R. Astron. Soc.*, 382 (2007) L72.
G. Ghisellini, G. Ghirlanda and L. Nava, *Mon. Not. R. Astron. Soc.*, 403 (2010) 926.
G. Ghirlanda, L. Nava and G. Ghisellini, arXiv:0908.2807 (2009).
G. Ghirlanda, G. Ghisellini and L. Nava, *Astron. Astrophys.*, 510 (2010) L7.
D. Giannios, *Astron. Astrophys.*, 480 (2008) 305.
D. Giannios and H. C. Spruit, *Astron. Astrophys.*, 469 (2007) 1.
M. M. González et al., *Nature*, 424 (2003) 749.
J. Goodman, *ApJ*, 308 (1986) L47.
J. Goodman and A. I. MacFadyen, *J. Fluid Mech.*, 604 (2008) 325.
J. Granot, J. Cohen-Tanugi and E. do Couto e Silva, *ApJ*, 677 (2008) 92.
O. M. Grimsrud and I. Wasserman, *Mon. Not. R. Astron. Soc.*, 300 (1998) 1158.
J. F. Grosse-Oetringhaus and K. Reygiers, arXiv:0912.0023 (2009).
D. Guetta, M. Spada and E. Waxman, *ApJ*, 557 (2001) 399.
K. Huang et al., *ApJ*, 654 (2006) L25.
K. Hurley et al., *Nature*, 372 (1994) 652.
K. Ioka, S. Kobayashi and B. Zhang, *ApJ*, 631 (2005) 429.
K. Ioka, K. Toma, R. Yamazaki and T. Nakamura, *Astron. Astrophys.*, 458 (2006) 7.
K. Ioka, K. Murase, K. Toma, S. Nagataki and T. Nakamura, *ApJ*, 670 (2007) L77.
D. Kazanas, M. Georganopoulos and A. Mastichiadis, *ApJ*, 578 (2002) L15.
T. M. Kneiske, T. Bretz, K. Mannheim and D. H. Hartmann, *Astron. Astrophys.*, 413 (2004) 807.
S. Kobayashi, T. Piran and R. Sari, *ApJ*, 490 (1997) 92.
S. Kobayashi and R. Sari, *ApJ*, 551 (2001) 934.
S. Kobayashi, F. Ryde and A. MacFadyen, *ApJ*, 577 (2002) 302.
Y. Kodama, D. Yonetoku, T. Murakami, S. Tanabe, R. Tsutsui and T. Nakamura, *Mon. Not. R. Astron. Soc.*, 391 (2008) L1.
P. Kumar, *ApJ*, 523 (1999) L113.
P. Kumar and R. Barniol Duran, *Mon. Not. R. Astron. Soc.*, 400 (2009a) L75.
P. Kumar and R. Barniol Duran, arXiv:0910.5726 (2009b).
D. Lazzati, G. Ghisellini, A. Celotti and M. J. Rees, *ApJ*, 529 (2000) L17.
D. Lazzati, E. Rossi, G. Ghisellini and M. J. Rees, *Mon. Not. R. Astron. Soc.*, 347 (2004) L1.
D. Lazzati, B. J. Morsony and M. Begelman, *ApJ*, 700 (2009) L47.
D. Lazzati and M. C. Begelman, arXiv:1005.4704 (2010).
A. Levinson and D. Eichler, *ApJ*, 594 (2003) L19.
Z. Li, *ApJ*, 709 (2010a) 525.
Z. Li, arXiv:1004.0791 (2010b).
Z. Li, Z. G. Dai, T. Lu and L. M. Song, *ApJ*, 599 (2003) 380.
E. W. Liang, S. x. Yi, J. Zhang, H. J. LV, B. B. Zhang and B. Zhang, arXiv:0912.4800 (2009).
Y. Lithwick and R. Sari, *ApJ*, 555 (2001) 540.
A. Mastichiadis and D. Kazanas, *ApJ*, 694 (2009) L54.
M. V. Medvedev and A. Loeb, *ApJ*, 526 (1999) 697.
M. V. Medvedev, *ApJ*, 540 (2000) 704.
P. Mészáros and M. J. Rees, *ApJ*, 405 (1993a) 278.
P. Mészáros and M. J. Rees, *ApJ*, 418 (1993b) L59.

- P. Mészáros and M. J. Rees, *ApJ*, 482 (1997) L29.
P. Mészáros and M. J. Rees, *ApJ*, 530 (2000a) 292.
P. Mészáros and M. J. Rees, *ApJ*, 541 (2000b) L5.
P. Mészáros, E. Ramirez-Ruiz, M. J. Rees and B. Zhang, *ApJ*, 578 (2002) 812.
A. Mizuta, S. Yamada and H. Takabe, *ApJ*, 606 (2004) 804.
A. Mizuta, S. Nagataki and J. Aoi, arXiv:1006.2440 (2010).
K. Murase, *PRD*, 78 (2008) 101302.
K. Murase and K. Ioka, *ApJ*, 676 (2008) 1123.
K. Murase, K. Toma, R. Yamazaki, S. Nagataki and K. Ioka, *Mon. Not. R. Astron. Soc.*, 402 (2010) L54.
E. Nakar, S. Ando and R. Sari, *ApJ*, 703 (2009) 675.
L. Nava, G. Ghirlanda, G. Ghisellini and A. Celotti, arXiv:1004.1410 (2010).
A. Neamus, arXiv:1005.1051 (2010).
J. P. Norris and J. T. Bonnell, *ApJ*, 643 (2006) 266.
M. Ohno, K. Ioka, K. Yamaoka, M. Tashiro, Y. Fukazawa and Y. E. Nakagawa, arXiv:0812.3737 (2008).
B. Paczyński, *ApJ*, 308 (1986) L43.
B. Paczyński and G. Xu, *ApJ*, 427 (1994) 708.
A. Panaitescu and P. Mészáros, *ApJ*, 544 (2000) L17.
A. Panaitescu, P. Mészáros, D. N. Burrows, J. Nousek, N. Gehrels, P. O'Brien and R. Willingale, *Mon. Not. R. Astron. Soc.*, 369 (2006) 2059.
S. B. Pandey et al., *ApJ*, 714 (2010) 799.
A. Pe'er and E. Waxman, *ApJ*, 613 (2004) 448.
A. Pe'er and B. Zhang, *ApJ*, 653 (2006) 454.
A. Pe'er, P. Mészáros and M. J. Rees, *ApJ*, 642 (2006) 995.
A. Pe'er, F. Ryde, R. A. M. Wijers, P. Mészáros and M. J. Rees, *ApJ*, 664 (2007) L1.
R. P. Pilla and A. Loeb, *ApJ*, 494 (1998) L167.
T. Piran and E. Nakar, arXiv:1003.5919 (2010).
J. Pruet, *ApJ*, 591 (2003) 1104.
J. L. Racusin et al., *Nature*, 455 (2008) 183.
S. Razzaque, P. Mészáros and E. Waxman, *PRD*, 68 (2003) 083001.
S. Razzaque, P. Mészáros and B. Zhang, *ApJ*, 613 (2004) 1072.
S. Razzaque, C. D. Dermer and J. D. Finke, arXiv:0908.0513 (2009).
M. J. Rees and P. Mészáros, *ApJ*, 430 (1994) L93.
M. J. Rees and P. Mészáros, *ApJ*, 628 (2005) 847.
E. Rossi and M. J. Rees, *Mon. Not. R. Astron. Soc.*, 339 (2003) 881.
F. Ryde, *ApJ*, 625 (2005) L95.
F. Ryde and A. Pe'er, *ApJ*, 702 (2009) 1211.
F. Ryde et al., *ApJ*, 709 (2010) L172.
E. S. Rykoff et al., *ApJ*, 702 (2009) 489.
R. Sari and A. A. Esin, *ApJ*, 548 (2001) 787.
R. Sari and T. Piran, *Mon. Not. R. Astron. Soc.*, 287 (1997a) 110.
R. Sari and T. Piran, *ApJ*, 485 (1997b) 270.
R. Sari and T. Piran, *ApJ*, 517 (1999a) L109.
R. Sari and T. Piran, *ApJ*, 520 (1999b) 641.
G. Sato et al., *ApJ*, 657 (2007) 359.
A. Shemi and T. Piran, *ApJ*, 365 (1990) L55.
L. Sironi and J. Goodman, *ApJ*, 671 (2007) 1858.
A. Spitkovsky, *ApJ*, 673 (2008) L39.
B. E. Stern and J. Poutanen, *Mon. Not. R. Astron. Soc.*, 352 (2004) L35.
R. Svensson, *Mon. Not. R. Astron. Soc.*, 227 (1987) 403.
M. Teshima, private communication (2010).
C. Thompson, *Mon. Not. R. Astron. Soc.*, 270 (1994) 480.
C. Thompson, *ApJ*, 651 (2006) 333.
C. Thompson, P. Mészáros and M. J. Rees, *ApJ*, 666 (2007) 1012.
K. Toma, K. Ioka, R. Yamazaki and T. Nakamura, *ApJ*, 640 (2006) L139.
K. Toma, K. Ioka, T. Sakamoto and T. Nakamura, *ApJ*, 659 (2007) 1420.
K. Toma, K. Ioka and T. Nakamura, *ApJ*, 673 (2008) L123.
K. Toma, X. F. Wu and P. Mészáros, *ApJ*, 707 (2009) 1404.
K. Toma, X. F. Wu and P. Mészáros, arXiv:1002.2634 (2010).
X. Y. Wang and Z. G. Dai, *ApJ*, 691 (2009) L67.
X. Y. Wang, Z. Li, Z. G. Dai and P. Mészáros, *ApJ*, 698 (2009) L98.
X. Y. Wang, H. N. He, Z. Li, X. F. Wu and Z. G. Dai, *ApJ*, 712 (2010) 1232.
E. Waxman and T. Piran, *ApJ*, 433 (1994) L85.
R. A. M. Wijers and T. J. Galama, *ApJ*, 523 (1999) 177.
D. Yonetoku, T. Murakami, T. Nakamura, R. Yamazaki, A. K. Inoue and K. Ioka, *ApJ*, 609 (2004) 935.
S. A. Yost et al., *ApJ*, 669 (2007) 1107.
B. Zhang and P. Mészáros, *ApJ*, 581 (2002) 1236.
B. Zhang, S. Kobayashi and P. Mészáros, *ApJ*, 595 (2003) 950.
B. Zhang et al., *ApJ*, 642 (2006) 354.
B. Zhang et al., *ApJ*, 655 (2007) 989.
B. Zhang and A. Pe'er, *ApJ*, 700 (2009) L65.
W. Q. Zhang, S. E. Woosley and A. Heger, *ApJ*, 608 (2004) 365.
W. Zhang, A. MacFadyen and P. Wang, *ApJ*, 692 (2009) L40.
Y. C. Zou, Y. Z. Fan and T. Piran, *Mon. Not. R. Astron. Soc.*, 396 (2009) 1163.
Y. C. Zou and T. Piran, *Mon. Not. R. Astron. Soc.*, 402 (2010) 1854.